# *CHAPTER 3*

## *Ab Initio*
## *ENERGETICS OF GALLIUM PNICTIDES*

## 3.1 Introduction

The importance of gallium was oversighted until it was fused with the elements of pnictide family; this unique combination has placed it amongst the group of most prestigious materials of the earth with respect to its applications to numerous cutting-edge technologies.[1–3] Emergence of such novel materials with nanostructured geometry has dramatically transformed the world into a techno-purpose place where everything is available on just a single click through a fingertip.[4] The trademark term *nano* here, refers to the subtle modifications in the material properties ranging from shape to structure and to almost all physical and chemical properties on imposition of dimensional confinement. Considering the material with foremost importance in the III-V family, the gallium arsenide (GaAs) that akin to its sibling III-V materials tend to get crystallized in cubic zincblende (ZB) structure with $F\bar{4}3m$ space group undergoes a pseudo phase transition or tend to acquire Wurtzite (WZ) crystal phase with hexagonal symmetry under confined geometries maintaining the same coordination number and packing fraction.[5,6] The hexagonal Wurtzite (WZ) as famously known to get crystallized with stacking sequence …ABABAB…., whereas its counterphase, i.e., cubic ZB is formed for the atomic stacking sequence …ABCABCABC… Although both polytypic phases have many similarities, but when the comparison comes to their properties, a clear line of demarcation is observed departing both phases with markable differences in the magnitudes and trends of the properties.[7–11] A plethora of research articles focusing on various properties of III-V compounds can be found,[12–35] demonstrating the diverse aspects of their utilization, and thus show that these compounds are nontrivial and should be investigated thoroughly for drawing a clear

picture of the transport properties. Gallium when combined with aluminium (Al) and nitrogen (N), forms a unique combination that bagged three Japanese scientists 'The Nobel Prize in Physics' for the year 2014.[36] Until then, the fabrication of white light emitting diode (LED) was not achieved due to limitations of the materials to produce blue light. Besides GaAs, other siblings like GaN, GaP, GaSb and GaBi have also received incomparable attention for their optoelectronic,[36] photovoltaic,[37–39] photocatalytic[40,41] and thermoelectric applications.[42,43] As mentioned earlier, the fundamental properties of these materials have been investigated theoretically[15,26,29,30,32,33,35] and experimentally,[12,13,16–22,24,27,28] yet a systematic evaluation and assessment of their properties in their polytypic phases (ZB and WZ) under bulk and conditional configurations were completely missing. For filling the gaps in the literature and for getting clear insight to the dynamics and mechanism of the properties of these compounds, we selected three gallium based pnictide compounds gallium phosphide (GaP), gallium arsenide (GaAs) and gallium antimonide (GaSb) for studying their properties under bulk and conditional configurations like dimensional confinement, size-effect, strained geometries, etc. The present chapter first gives systematic account on the polytypic phase (ZB and WZ) dependent structural, electronic, vibrational, thermal and thermoelectric properties of the selected GaX (X=P, As, Sb) compounds. The later part of the chapter describes the results on the structural, electronic and optical properties of the nanostructured GaX compounds with one-dimensional nanowire (1D NW) geometry. Further, to get the insight to the electro-optic transport under conditional environment like size-effect and external strain, the properties are re-calculated under modified conditions, and

the results are compared to get complete blue print of the electro-optic properties of GaX compounds.

## 3.2 Computational Details

### 3.2.1 Bulk crystal structures

Initially, the three III-V compounds namely, GaP, GaAs and GaSb in cubic ZB and hexagonal WZ phases were constructed by assigning correct Wyckoff positions to the anions and cations in the preferred unitcell. The unitcells were then considered for optimizing the ionic positions, angles, bond-lengths, lattice parameters, etc., under self-consistent total-energy minimization process. The *state-of-the-art* density functional theory (DFT)[44] formalism was incorporated for optimizing the crystal structures of the compounds and for the computation of the ground state structural, electronic, vibrational, thermal and thermoelectric properties of the gallium pnictides generally termed as GaX here. The valence electronic configurations for Ga ($4s^24p^1$), P ($3s^23p^3$), As ($4s^24p^3$), and Sb ($5s^25p^3$) atomic species were configured under norm-conserving pseudopotentials. To treat the exchange and correlation effects, the Perdue and Zunger parameterized local density approximation (LDA) based functionals were incorporated for solving the many body Kohn-Sham equation.[45] To confirm the well-converged parameters, the threshold for the convergence of total-energy between two consecutive electronic iterative steps was kept at $10^{-5}$ eV with maximum Hellman-Feynman forces acting on each atom reduced to 0.001 eV/Å. The high magnitude of kinetic energy cut-off of 1200 eV for the electronic wave-function with dense Monkhorst-Pack scheme[46] based k-mesh grids of densities 16x16x16 for ZB and 16x16x10 for WZ compounds were found to be suitable for obtaining well converged

parameters. The optimized crystal structures then were used for the computation of all proposed ground state properties. The electronic dispersion curve, total and partial density of states (PDOS) are computed to get insight to electronic transport. For validation of the dynamic stability of the systems and for computing thermal and thermoelectric transport properties, the density functional perturbation theory (DFPT)[47] is utilized and phonon dispersion curves (PDCs) with phonon density of states (PHDOS) are computed under linear response approach. The inverse Fourier transformation for obtaining exact phonon frequencies at corresponding eigenvectors is performed with compatible **q**-mesh grids of densities 6 x 6 x 6 and 6 x 6 x 4 for ZB and WZ phases, respectively. The unique thermodynamic functions such as specific heat ($C_v$), Debye temperature ($\Theta_D$), entropy (S), internal and vibrational energies of GaX compounds are evaluated using the equations below under quasi-harmonic approximation (QHA).

$$E(T) = E_{tot} + E_{zp} + \int \frac{\hbar\omega}{\exp\left(\frac{\hbar\omega}{kT}\right) - 1} F(\omega) d\omega \tag{3.1}$$

$$F(T) = E_{tot} + E_{zp} + kT \int F(\omega) \ln\left[1 - \exp\left(-\frac{\hbar\omega}{kT}\right)\right] d\omega \tag{3.2}$$

$$S(T) = \mathrm{k}\left\{\int \frac{\hbar\omega}{\exp\left(\frac{\hbar\omega}{kT}\right)-1} F(\omega) d\omega - \int F(\omega)\left[1 - \exp\left(-\frac{\hbar\omega}{kT}\right)\right] d\omega\right\} \tag{3.3}$$

$$\mathrm{C_v(T)} = k \frac{\int \left(\frac{\hbar\omega}{kT}\right)^2 \exp\left(\frac{\hbar\omega}{kT}\right)}{[\exp\left(\frac{\hbar\omega}{kT}\right) - 1]^2} F(\omega) d\omega \tag{3.4}$$

Here, the terms $E_{tot}$ and $E_{zp}$ are respectively the total-energy and the zero-point energy, $\hbar$ is reduced Plank's constant and, F(ω) represents the phonon density of states (PHDOS) function. Moving towards the computations of thermoelectric properties, the term figure of merit (ZT) that replicates the overall performance/thermoelectric power conversion efficiency of any material is assessed from the equations below:

$$ZT_e = \left(\frac{S^2\sigma}{\kappa_e}\right)T \tag{3.5}$$

$$ZT = \left(\frac{S^2\sigma}{\kappa_e + \kappa_l}\right)T \tag{3.6}$$

Here, S is Seebeck co-efficient, σ is electrical conductivity, T is temperature and $\kappa_e$ and $\kappa_l$ are the electronic and lattice contributions to the thermal conductivity, respectively with the terms $ZT_e$ and ZT being the electronic and overall figure of merits, respectively. The detailed methodology for computing the thermoelectric properties is described in **CHAPTER 2**.

### 3.2.2 One-Dimensional Nanostructures: The Nanowires

As discussed earlier, most of the III-V compounds are found to get crystallized in cubic ZB phase, and under confined dimensions, the formation of the nanostructures is found to be more stable under the polytypic WZ phase with hexagonal symmetry.[10,48] Therefore, to understand the electro-optic transport through the one-dimensional (1D) nanostructures of the GaX compounds (nanowires (NWs)), the study was limited to the hexagonal WZ phase only. For construction of the NWs, the optimized bulk WZ

crystal structure of GaX compounds were considered for generating supercells. The supercells of the GaX compounds were constructed by repeating the unitcells in 001, 010 and 001 directions, and, then, by framing the required diameter of the corresponding NWs, the supercells were cut along the **z** direction for obtaining the GaX NWs unitcells with three distinct diameters with nine NW unitcells in total. The lateral surfaces of these bare NWs were masked with the pseudo hydrogen adatoms to remove surface dangling bond effects. To avoid interactions between the non-periodic images of the NW unitcells, a vacuum slab of 15 Å thickness was inserted in the **x** and **y** directions. The fully saturated NWs of GaX compounds with three distinct diameters were then considered for optimizing all parameters as mentioned for bulk compounds. In the case of NWs, the **k**-mesh grid of 1x1x8 and kinetic energy cut-off of 850 eV were found sufficient enough to converge the total-energy within the prescribed criteria. The structural stability of the NWs is assessed by means of computing the formation energy.

$$E_{FORM}^{NW} = \frac{E_{Tot} - m\mu_{Ga} - n\mu_X - l\mu_H}{m + n + l} \tag{3.7}$$

Here, the terms $E_{FORM}^{NW}$ and $E_{Tot}$ represent the formation energy and total-energy of the NWs and $\mu_{Ga}, \mu_X$and $\mu_H$ represent the respective chemical potentials of the Ga, X=P, As, Sb and H atom with total number of corresponding atoms per unit cell labelled as m, n and l, respectively. Apart from the electronic transport, the complex di-electric function $\varepsilon(\omega)$ of the NWs are computed under random phase approximation (RPA)[49,50] for the evaluation of optical transport through the NWs (see **CHAPTER 2** for details).

## 3.3 Results and Discussion

The present chapter deals with the computation of the ground state properties of the GaX compounds in its bulk polytypic phases, and in two-dimensionally confined 1D NW configuration to assess the effect of phase dependent and confinement dependent modifications in the properties. The section 3.3.1 provides complete picture of electronic to thermoelectric transport properties through the polytypic phases of the GaX compounds, while the section 3.3.2 covers the results on the electro-optic transport properties of the two-dimensionally confined GaX compounds.

### 3.3.1 Ground State Properties of GaX Compounds in Bulk Polytypes

#### 3.3.1.1 Structural Properties

Differing from the stacking of atomic layers, the cubic ZB and hexagonal WZ crystal structures of GaX compounds also possess difference in the space groups ($F\bar{4}3m$ (ZB) and $P6_3mc$ (WZ)) and atomic contributions responsible for the modulation in their electronic and vibrational dispersion curves. The DFT computed lattice parameters of the GaX compounds are listed in Table 3.1. The results show that our LDA predicted lattice parameters are slightly underestimated (1.2-2%) than the reported experimental values,[16,17,51] which can be correlated with the over binding of the atoms by 1-2% under the treatment.[52] However, the good agreement of the c/a ratio for WZ compounds with slight deviation of 0.9% results in agreement between the computed and reported values of bulk modulus (see Table 3.1). As per the trend, increase in anion mass causes enhancement in the lattice parameters, whereas, the reverse is observed for bulk modulus. The good agreement between the experimental data with the computed parameters validate the pseudopotentials and the exchange-

correlation functionals incorporated for the computation of the ground state properties.[51]

**Table 3.1. The lattice parameters, bulk modulus and pressure derivative of bulk modulus of GaX compounds in ZB and WZ phases.**

| System | Property | Lattice parameter (Å) | | | Bulk modulus (GPa) | | Pressure derivative of bulk modulus | |
|---|---|---|---|---|---|---|---|---|
| | Phase | ZB | WZ | | ZB | WZ | ZB | WZ |
| | Parameter | a | A | c/a | | $B_0$ | $B_0'$ | |
| GaP | Present | 5.338 | 3.762 | 1.649 | 91.5 | 88.8 | 4.40 | 4.41 |
| | **Exp.** | **5.451**[a] | **3.842**[b] | **1.649**[c] | **88**[a] | - | - | - |
| | Other | 5.332[d] | 3.763[d] | 1.639[d] | 92.1[d] | 91.23[d] | 4.339[d] | 4.3437[d] |
| | | 5.43[e] | 3.800[k] | 1.650[k] | 91.9[e] | | 4.58[e] | |
| | | 5.41[f] | | | 91.5[f] | | 4.50[f] | |
| | | 5.54[g] | | | 79.1[g] | | 4.45[g] | |
| | | 5.52[h] | | | 77.3[h] | | 4.52[h] | |
| | | 5.501[i] | | | 77.21[i] | | 4.88[i] | |
| | | 5.451[j] | | | | | | |
| | | 5.397[k] | | | | | | |
| | | | | | | | | |
| GaAs | Present | 5.547 | 3.909 | 1.649 | 75.4 | 74.1 | 4.52 | 4.53 |
| | **Exp.** | **5.649**[a] | **4.021**[c] | - | **77**[a] | - | - | - |
| | Other | 5.530[d] | 3.912[d] | 1.637[d] | 75.7[d] | 74.73[d] | 4.487[d] | 4.5048[d] |
| | | 5.63[e] | 3.953[k] | 1.650[k] | 77.1[e] | | 4.30[e] | |
| | | 5.61[f] | | | 76.0[f] | | 4.33[f] | |
| | | 5.77[g] | | | 64.4[g] | | 4.86[g] | |
| | | 5.75[h] | | | 60.2[h] | | 5.20[h] | |
| | | 5.733[i] | | | 60.83[i] | | 4.60[i] | |
| | | 5.653[j] | | | | | | |
| | | 5.440[k] | | | | | | |
| | | | | | | | | |
| GaSb | Present | 6.005 | 4.232 | 1.648 | 56 | 55.4 | 4.64 | 4.64 |
| | **Exp.** | **6.081**[a] | - | - | **56**[a] | - | - | - |
| | Other | 5.981[d] | 4.234[d] | 1.635[d] | 56.7[d] | 55.80[d] | 4.662[d] | 4.6695[d] |
| | | 6.08[e] | 4.233[k] | 1.653[k] | 60.0[e] | | 4.78[e] | |
| | | 6.06[f] | | | 56.6[f] | | 4.80[f] | |
| | | 6.24[g] | | | 49.1[g] | | 4.66[g] | |
| | | 6.22[h] | | | 45.9[h] | | 4.16[h] | |
| | | 6.193[i] | | | 45.92[i] | | 5.16[i] | |
| | | 6.118[j] | | | | | | |
| | | 6.018[k] | | | | | | |

[a]Ref.[51] [Exp] [e-h]Ref.[33] [LDA and GGA]
[b]Ref.[17] [Exp] [i]Ref.[29] [GGA]
[c]Ref.[16] [Exp] [j]Ref.[32] [Empirical Method]
[d]Ref.[26] [LDA] [k]Ref.[30] [LDA]

### 3.3.1.2 Electronic Properties

The ground state electronic properties of the III-V semiconductors that are known for being well predicted by the Kohn-Sham DFT formulism with LDA pseudopotentials[52]

**Table 3.2. The electronic bandgaps and bandgap types of GaX compounds in ZB and WZ phases.**

| *System* | | **Energy band gap (eV)** | | | | **Bandgap Type** | |
|---|---|---|---|---|---|---|---|
| | | **ZB** | | | **WZ** | **ZB** | **WZ** |
| | | $E_g^{\Gamma-\Gamma}$ | $E_g^{\Gamma-X}$ | $E_g^{\Gamma-L}$ | $E_g^{\Gamma-\Gamma}$ | | |
| *GaP* | | | | | | | |
| | Present | 2.632 | 1.4328 | 1.9652 | 1.5895(1.3987) | Indirect | Indirect |
| | **Exp.** | **2.78[a]** | **2.26[a]** | **2.6[a]** | **2.09[k]** | | |
| | Other | 2.29[e] | 2.55[e] | 3.25[e] | 1.4389[g] | | |
| | | 1.46[f] | 1.68[f] | 1.51[f] | 2.251[j] | | |
| | | 2.438[g] | - | - | | | |
| | | 2.0[h] | 2.50[h] | 2.09[h] | | | |
| | | 2.774[i] | 2.25[i] | 2.6[i] | | | |
| | | 2.47[m] | | | | | |
| | | 2.85[m] | | | | | |
| | | | | | | | |
| *GaAs* | Present | 1.3542 | 1.3391 | 1.3391 | 1.0615 | Direct | Direct |
| | **Exp.** | **1.42[b]** | **1.81[b]** | **1.72[b]** | **1.459[l]** | | |
| | Other | 1.21[e] | 2.32[e] | 1.65[e] | 0.7781[g] | | |
| | | 0.05[f] | 1.49[f] | 0.79[f] | 1.503[j] | | |
| | | 1.008[g] | - | - | | | |
| | | 0.49[h] | 2.40[h] | 1.3[h] | | | |
| | | 1.42[i] | 1.81[i] | 1.72[i] | | | |
| | | 1.21[m] | | | | | |
| | | 1.44[m] | | | | | |
| | | | | | | | |
| *GaSb* | Present | 0.678 | 0.8156 | 0.6086 | 0.3359 | Direct | Direct |
| | **Exp.** | **0.725[c]** | **1.03[d]** | **0.761[d]** | **-** | | |
| | Other | 1.00[e] | 1.46[e] | 1.13[e] | 0.1673[g] | | |
| | | -0.35[f] | 0.94[f] | 0.28[f] | 0.509[j] | | |
| | | 0.547[g] | - | - | | | |
| | | 0.4[h] | 1.60[h] | 0.8[h] | | | |
| | | 0.715[i] | 1.012[i] | 0.777[i] | | | |
| | | 0.72[m] | | | | | |
| | | 0.81[m] | | | | | |

[a]Ref.[40] [Exp]
[b]Ref.[13] [Exp]
[c]Ref.[28] [Exp]
[d]Ref.[12] [Exp]
[e-f]Ref.[33][LDA and GGA]
[g]Ref.[26][LDA]
[h]Ref.[29][GGA]
[i]Ref.[32] [Empirical Method]
[j]Ref.[35] [Empirical Method]
[k]Ref.[24][Exp]
[l]Ref.[18][Exp]
[m]Ref.[53][Hybrid Functional]

are listed in Table 3.2, and the electronic dispersion curves solved within first Brillouin zone through integration of electronic states along high-symmetry points are presented in Figure 3.1. The respective available energy states per unit energy, i.e. PDOS plots are shown in Figure 3.2. As it can be observed from the Figs. 3.1 (a-f) and Table 3.2, as the anion mass increases, the electronic bandgap reduces with values 1.43 eV, 1.35 eV and 0.65 eV in ZB and 1.39 eV, 1.06 eV and 0.33 eV in WZ phases, for GaP, GaAs and GaSb, respectively. For optoelectronic devices, it is desired that the material

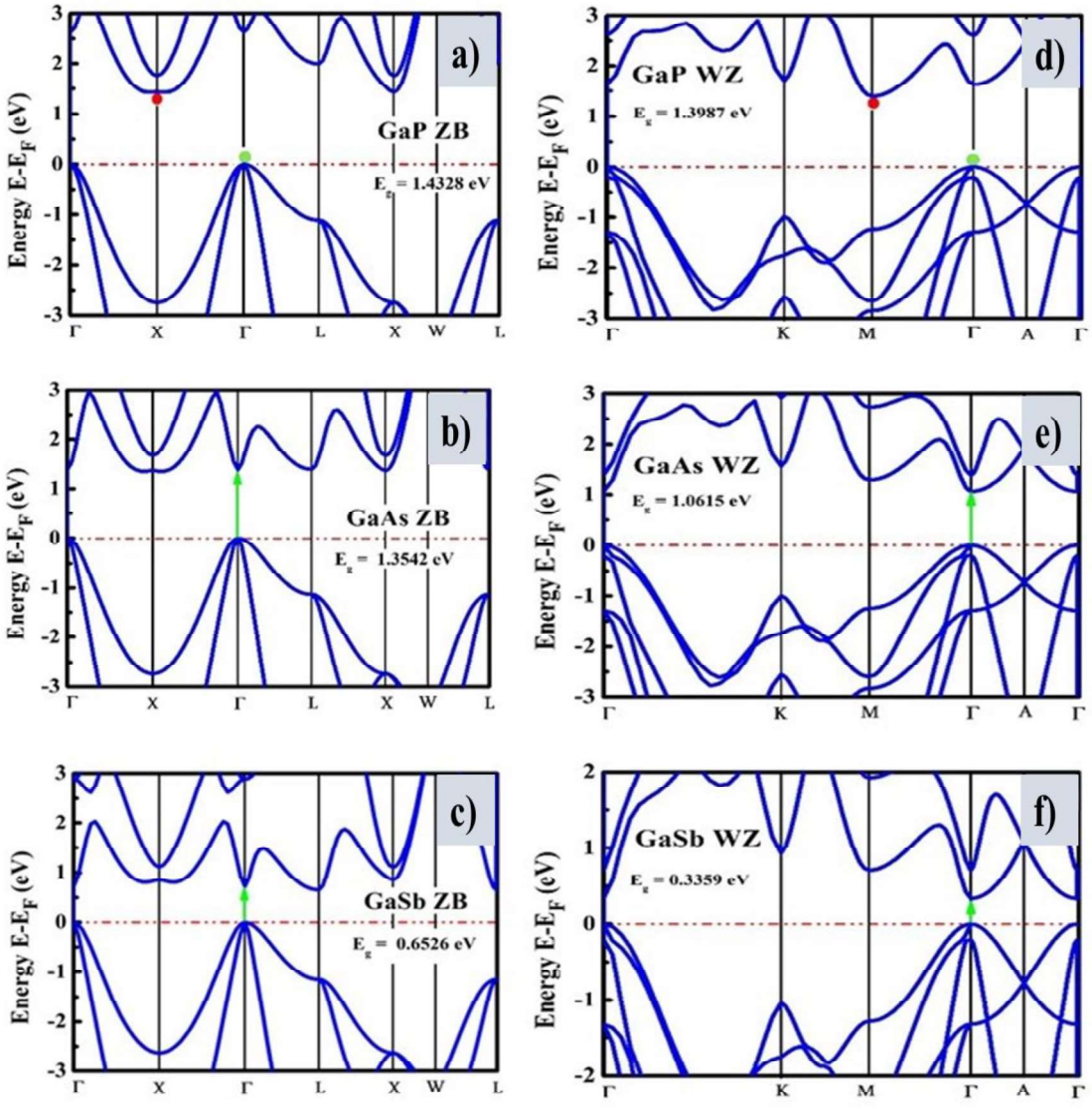


**Figure 3.1. The DFT computed electronic dispersion curves for (a, d) GaP, (b, e) GaAs and (c, f) GaSb in ZB and WZ phases, respectively.**

should possess direct electronic bandgap with magnitude lying within the range of optical spectra in electromagnetic spectrum. Amongst all compounds, except GaP, both the compounds GaAs and GaSb possess direct nature in both polytypic phases. It is noteworthy, that the computed electronic bandgaps for GaX compounds are in good agreement with the reported data[13,19,28] with slight underestimation which is

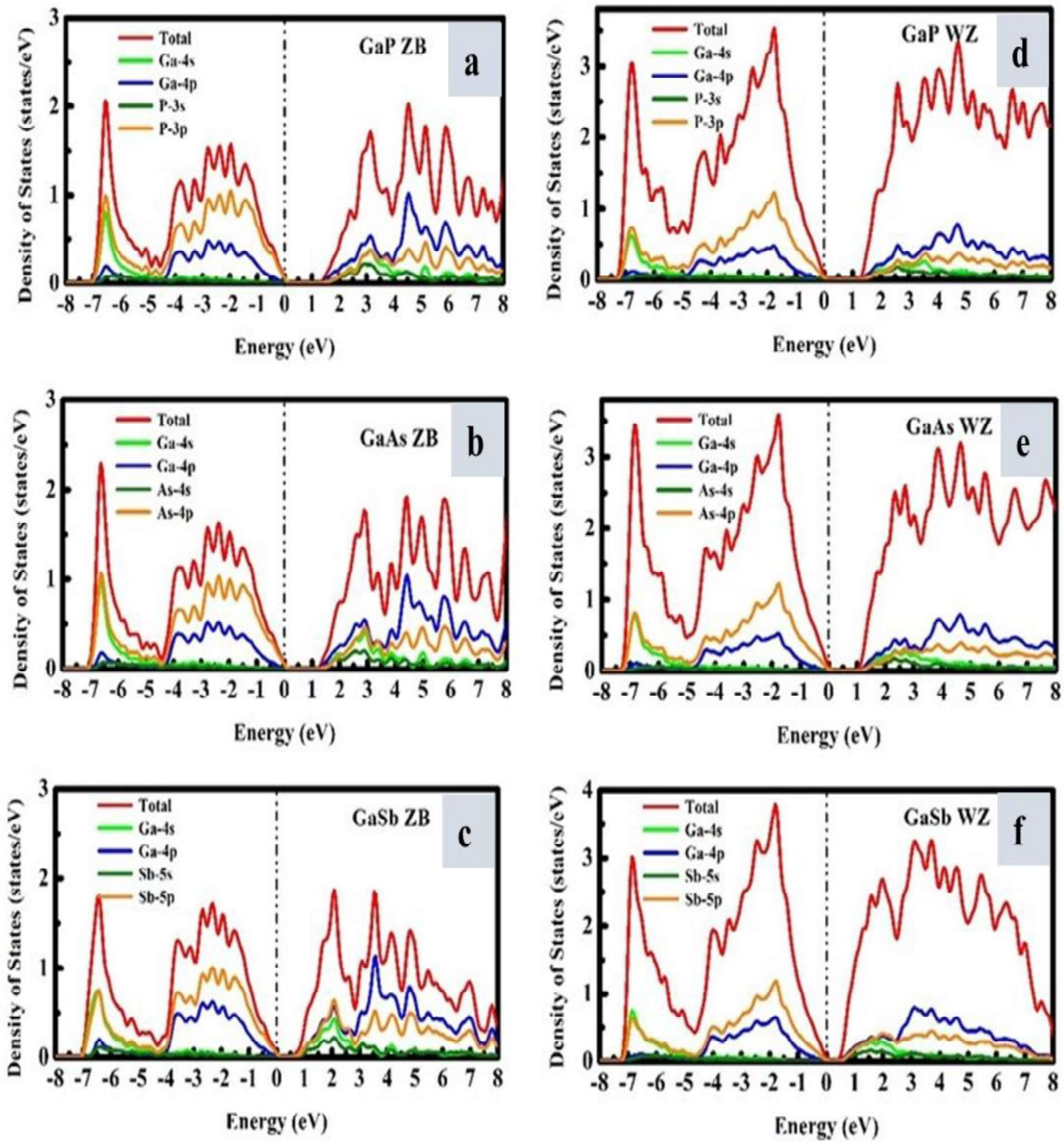


**Figure 3.2. The computed electronic density of states (PDOS) plots as a function of energy for (a, d) GaP, (b, e) GaAs and (c, f) GaSb in ZB and WZ phases, respectively.**

intrinsic property of local density approximated (LDA) pseudopotentials. The projected density of states (PDOS) plots not only replicate the spatially distributed electronic states, but also reveal the information of the hybridization between the orbitals, nature of electronic bonds, and charge transfer mechanism between the atomic species. Figs. 3.2 (a-f) clearly indicate major contribution of Ga-*4p* electrons within the conduction band regime suggesting domination of electronic conduction, while, the valence band regime seems to be populated by the anion P-*3p*, As-*4p* and Sb-*5p* electrons for GaP, GaAs and GaSb, respectively. Akin to the electronic dispersion curves (Figs. 3.1(a-f)), the PDOS plots validate reduction in bandgap on increase in anion mass. Further, comparing both phases, the WZ compounds show much lower gap than the ZB counterparts subjected to enhanced number of electrons and stacking difference. Apart from the gap, the trend of the electronic dispersion curves also show difference in the curvature that in turn cause variation in the carrier effective masses, and with larger slope near the Fermi level, the ZB compounds are likely to possess lower carrier effective masses than the WZ counterpart. The tuning of the carrier effective mass is also one of the key parameters for achieving tailor made transport properties owing to its relation with carrier mobility $\mu$ and carrier relaxation time $\tau$.

#### 3.3.1.3 Vibrational Properties

The phonon dispersion curves (PDCs) of any material not only helps to reveal undergoing vibrational mechanism, but also give insight to the factors governing the vibrational dynamics. The PDCs are nothing but the pictorial representation of phonon vibrational frequencies corresponding to spatial reciprocal wave-vector **k** in

the wedge of irreducible Brillouin zone. All six PDCs presented in Figure 3.3 for GaP (a, d), GaAs (b, e) and GaSb (c, f) compounds with ZB and WZ phases, respectively indicate absence of imaginary frequency of the phonon modes. This observation

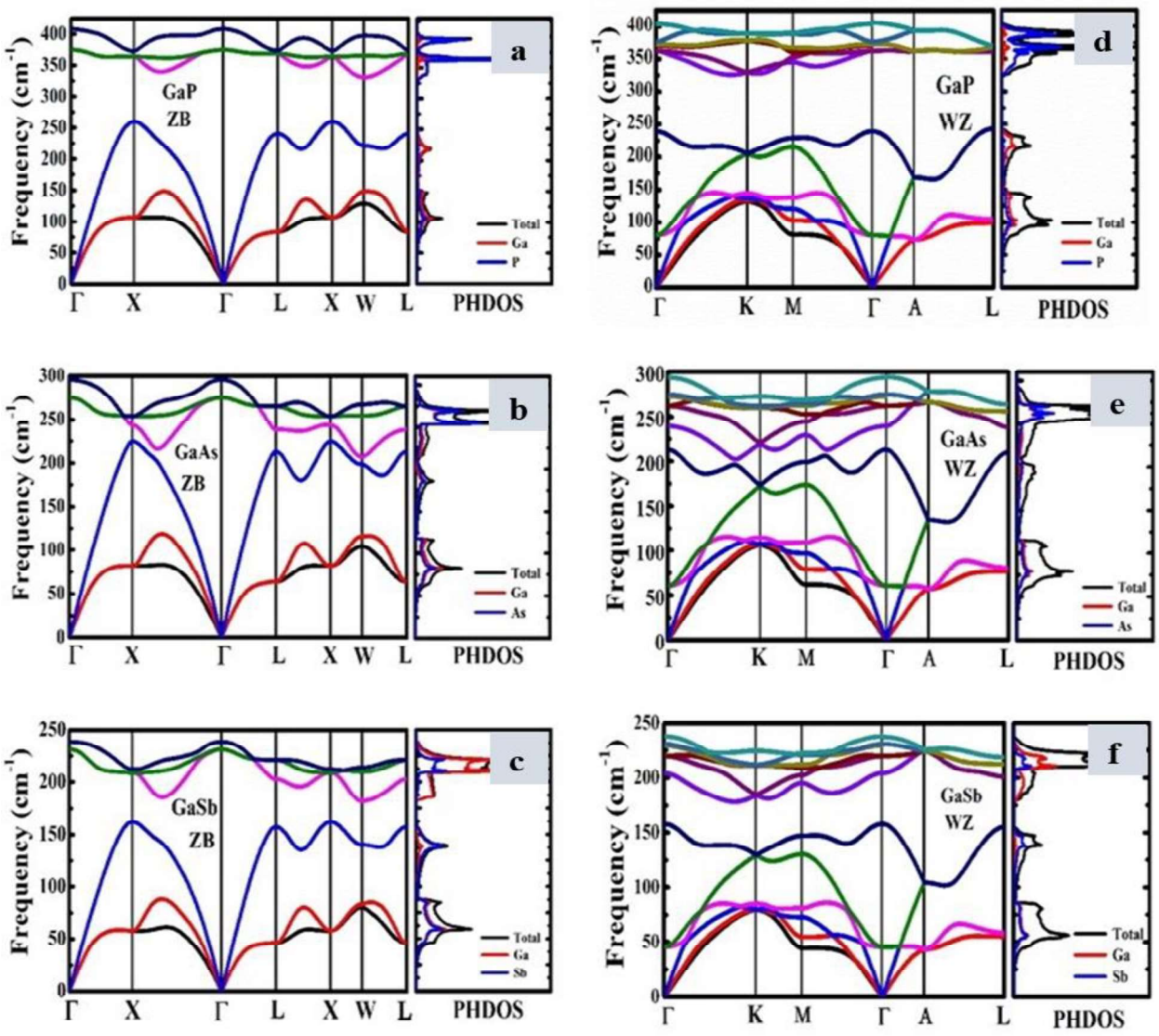


**Figure 3.3. The DFPT computed phonon dispersion curves (PDCs) and respective phonon density of states (PHDOS) curves for (a, d) GaP, (b, e) GaAs and (c, f) GaSb in ZB and WZ phases, respectively.**

validates the dynamical stability of GaX compounds in both polytypic phases. Viewing the respective PHDOS plots that showcase individual atomic contributions to the phonon modes suggest that the anions of the GaX compounds are the major contributors for the optic phonon modes owing to their low atomic mass; whereas, in

case of acoustic phonon modes, the cation Ga due to its heavy nature dominates the acoustic phonon modes. It is noteworthy, that the GaAs due to low mass anisotropy between its anion and cation species shows almost equally contributed phonon density within acoustic and optic phonon regimes. Looking at the alignment of phonon branches, apart from three acoustic phonon branches, the optic phonon modes in the ZB and WZ compounds are distributed with three and nine phonon branches, respectively. As the GaX compounds have significant amount of mass anisotropy, and the difference in the vibrational frequencies that is generated due to mechanical vibrations of the anions and cations, there arises degeneracy in the longitudinal optic (LO) and transverse optic (TO) phonon modes that is most prominent property of polar semiconductors.[54] The degeneracy can be measured via the difference, also known as the LO-TO splitting, shows decrease in both polytypes as we move from GaP, to GaAs, and to GaSb due to increase in anion mass and hence, decrease in degeneracy factor. As far as degeneracy of acoustic phonon modes is concerned, the all three acoustic modes; i.e., one longitudinal acoustic (LA) and two transverse acoustic (TA) modes are triply degenerate at the $\Gamma$ point of the Brillouin zone, and, while moving towards the other high-symmetry points of the Brillouin zone, the degeneracy between them consequently decreases and, the LA mode attains maximum magnitude of frequency at X point in case of ZB compounds. In case of WZ compounds, it can be observed (Figs. 3.3 (d-f)) that the three acoustic modes show similar behaviour along 0001 direction as that of ZB compounds along 111 direction, with few new phonon modes arising due to double number of atoms per unit cell. To have a comparative analysis, the unique frequencies of phonon modes at high-

symmetry points are listed in Tables 3.3 and 3.4 for ZB and WZ compounds, respectively. The assignment of phonon modes is evaluated by applying group theory analysis, which reveals that in case of WZ compounds, there are in total eight phonon modes arising at Γ point (zone center) of the Brillouin zone. These include $2A_1$, $2B_1$, $2E_1$ and $2E_2$ modes out of which the $B_1$ modes are silent modes.[55] The non-polar $E_2^h$ mode which is the signature phonon mode for WZ compounds,[30] is located at 368, 268 and 227 $cm^{-1}$ for GaP, GaAs and GaSb, respectively. The DFPT[47] predicted phonon frequency of 362 $cm^{-1}$ for GaP corresponds to the degenerate $E_1$(TO) and $A_1$(TO) modes shows excellent agreement with the experimentally observed frequency of 361 $cm^{-1}$ for both modes,[22] though the prior LDA based *first-principles* calculations is found in disagreement with the experimentally observed frequency, and exhibits a markable gap of 5 $cm^{-1}$ between these two modes.[30]

**Table 3.3. The acoustic and optic phonon frequencies at high-symmetry points of BZ, the Born effective charges ($Z^*$) and high frequency di-electric constants (ε) for ZB GaX compounds.**

| System | | $\Gamma_{TO}$ | $\Gamma_{LO}$ | $X_{TA}$ | $X_{LA}$ | $X_{TO}$ | $X_{LO}$ | $L_{TA}$ | $L_{LA}$ | $L_{TO}$ | $L_{LO}$ | $Z^*$ | ε |
|---|---|---|---|---|---|---|---|---|---|---|---|---|---|
| GaP | **Calc.** | 371 | 405 | 103 | 257 | 363 | 372 | 80 | 236 | 368 | 373 | 2.06 | 9.80 |
| | **Exp.**[a,b,e] | 366 | 404 | 103 | 250 | 379 | 358 | 64 | 212 | 353 | 368 | 2.04 | 9.11[g] |
| | **Other**[c] | 364 | 394 | 93 | 247 | 361 | 366 | 68 | 228 | 362 | 370 | 2.06 | 8.93 |
| | | | | | | | | | | | | | |
| GaAs | **Calc.** | 275 | 295 | 81 | 224 | 243 | 253 | 63 | 212 | 238 | 265 | 2.03 | 11.50 |
| | **Exp.**[d,e] | 271 | 293 | 82 | 225 | 257 | 240 | 63 | 207 | 264 | 242 | 2.07 | 10.9[g] |
| | **Other**[c,h] | 270 | 286 | 85 | 220 | 256 | 243 | 70 | 209 | 265 | 240 | 2.08 | 10.83 |
| | | 271 | 291 | 82 | 223 | 254 | 240 | 63 | 210 | 263 | 238 | 2.07 | 12.3 |
| GaSb | | | | | | | | | | | | | |
| | **Calc.** | 230 | 238 | 57 | 162 | 209 | 212 | 46 | 157 | 203 | 221 | 1.62 | 15.89 |
| | **Exp.**[f] | 224 | 233 | 57 | 166 | 212 | 212 | 46 | 153 | 205 | 216 | 2.15 | 14.4 |
| | **Other**[c,h] | 228 | 234 | 64 | 161 | 213 | 214 | 53 | 157 | 223 | 207 | 1.61 | 12.87 |
| | | 230 | 237 | 57 | 162 | 210 | 211 | 45 | 157 | 203 | 221 | 1.73 | 18.1 |

[a]Ref.[34] [Exp] [c]Ref.[30] [LDA] [e]Ref.[21] [Exp] [g]Ref.[23] [Exp]
[b]Ref.[56] [Exp] [d]Ref.[25] [Exp] [f]Ref.[14] [Exp] [h]Ref.[47] [LDA]

The frequencies of other phonon modes are slightly deviated from the experimental values; whereas, for GaAs, we observed excellent agreement with the reported experimental data.[27] There are no experimental data on vibrational profile of bulk GaSb with WZ phase, thus, the comparison of the obtained results is done with the prior DFT based data[30] which are in good agreement with the present results. The slight deviation observed in the phonon frequencies of GaX compounds is attributed to exclusion of *d-orbital* electrons in the pseudopotentials of the respective atomic species. The exclusion of the *d-orbital* electrons reduces screening effects, thus overestimating the bonding strength.[47]

**Table 3.4. The vibrational frequencies of phonon modes, Born effective charges ($Z^*$) and high frequency di-electric constants (ε) of WZ GaX compounds.**

| System | | Zone Center Phonon frequency ($cm^{-1}$) | | | | | | | | Effective Charge | Di-electric Constant |
|---|---|---|---|---|---|---|---|---|---|---|---|
| | | $E_2^1$ | $B_1^1$ | $A_1(TO)$ | $E_1(TO)$ | $E_2^h$ | $B_1^h$ | $A_1(LO)$ | $E_1(LO)$ | $Z^*$ | ε |
| **GaP** | Calc. | 78 | 236 | 362 | 362 | 368 | 375 | 407 | 402 | 2.019 | 9.75 |
| | **Exp.**[b] | 80 | 215 | 361 | 361 | 353 | 383 | 391 | 397 | - | - |
| | Other[a] | 76 | 232 | 361 | 366 | 358 | 375 | 413 | 393 | 2.64 | 8.93 |
| **GaAs** | Calc. | 59 | 211 | 239 | 262 | 261 | 274 | 293 | 294 | 1.98 | 11.14 |
| | **Exp.**[c] | 59 | 206 | - | 267 | 259 | 234 | 291 | - | - | - |
| | Other[a] | 59 | 207 | 267 | 271 | 261 | 239 | 287.5 | 287 | 2.01 | 10.82 |
| **GaSb** | Calc. | 43 | 156 | 219 | 202 | 227 | 229 | 239 | 236 | 1.57 | 14.67 |
| | Other[a] | 39 | 157 | 226 | 228 | 220 | 204 | 233 | 234 | 1.55 | 12.87 |

[a] Ref.[30][LDA]
[b]Ref.[22][Exp]
[c]Ref.[27][Exp]

The Born effective charge $Z^*$ and high frequency di-electric constants ε for ZB and WZ phases of GaX compounds are listed in Tables 3.3 and 3.4, respectively. The Born effective charge $Z^*$ is used for quantifying the coupling arising due to the interaction of the optic phonons and the electric field, which is found to be isotropic for cubic ZB phase as $Z^*_{xx} = Z^*_{yy} = Z^*_{zz}$, whereas, the same shows anisotropic nature for WZ phase as $Z^*_{xx} = Z^*_{yy} \neq Z^*_{zz}$. For comparison purpose, the average Born effective charge for both the phases is enlisted in the in Tables 3.3 and 3.4, respectively, which show excellent agreement with the reported experimental data for ZB compounds. The average values of high frequency di-electric constant ε show mass dependent trend in both phases, as it shows enhancement with increase in the anion mass. Further, for ZB compounds, the ε is slightly overestimated from the reported experimental data.[23] The reason for the overestimation is explained elsewhere and is in agreement with the observed trend.

### 3.3.1.4 Thermal and Thermoelectric Properties

The thermodynamic functions like lattice specific heat ($C_v$), Debye temperature($\Theta_D$), entropy (S), internal and vibrational energies of GaX compounds in both phases are computed to investigate the thermal profiles of the compounds and to validate their thermal stability. These volume dependent thermodynamic functions are shown in Figs. 3.4 and 3.5 for ZB and WZ phases, respectively. The QHA computed thermodynamic functions follow classical trends in both phases. The normalized specific heat approaches 3R at higher temperature, with R as a universal gas constant. The trend validates Dulong-Petit law, and at low temperature shows $T^3$ dependence validating Debye's law. Moving towards the assessment of the phase dependent

thermoelectric transport properties, the contributions from two distinct sources, i.e. electrons and phonons has been calculated individually for understanding the role of both carriers towards overall transport properties. The ability of a material to convert

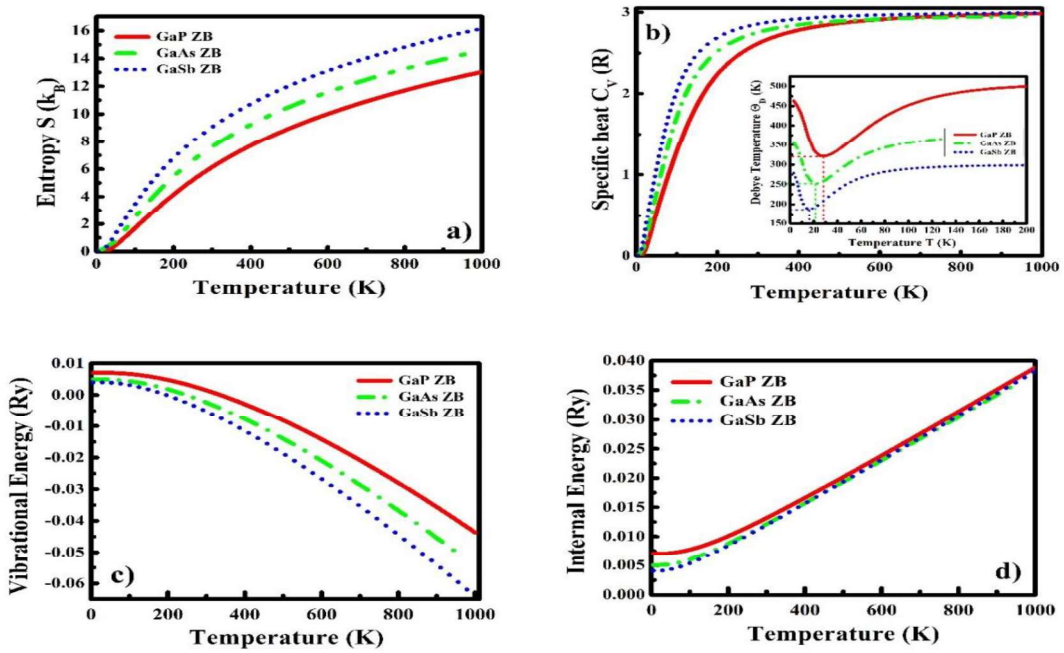


**Figure 3.4. QHA computed thermodynamic functions (a) Entropy, (b) Specific heat, (c) Vibrational Energy and (d) Internal energy of GaX compounds in ZB phase.**

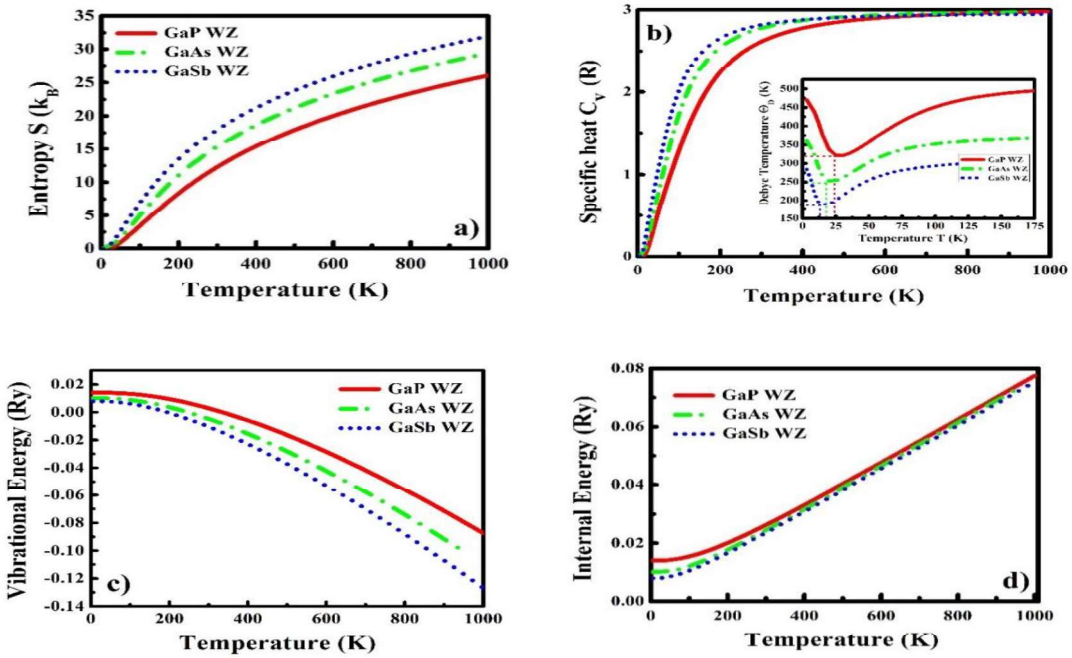


**Figure 3.5. QHA computed thermodynamic functions (a) Entropy, (b) Specific heat, (c) Vibrational Energy and (d) Internal energy of GaX compounds in WZ phase.**

heat to electric energy can be quantified by means of computing the thermoelectric efficiency which is defined by ZT (see **Computational Details**). The semi-classical Boltzmann Transport theory that accounts for the electronic contributions to the thermoelectric transport has been utilized for computing the carrier density and temperature dependent Seebeck co-efficient (s), electrical conductivity (σ) and electronic contribution to thermal conductivity ($\kappa_e$). The results are depicted in Figs. 3.6 and 3.7 for ZB and WZ compounds, respectively. As a known fact, the semi-classical treatment employed for solving Boltzmann transport equation for electrons with constant relaxation time approximation (CRTA) gives carrier relaxation time τ dependent thermoelectric transport properties,[57] the accurate prediction of the relaxation time is necessary for computing accurate magnitudes of the Seebeck co-efficient (S), electrical conductivity (σ), electronic thermal conductivity ($\kappa_e$), etc. To address this issue and for computing carrier relaxation time, the deformation potential theory[58] (see **CHAPTER 2**) has been employed, which first accounts carrier mobility μ to finally yield relaxation time τ. The calculated parameters for evaluating relaxation time are listed in Table 3.5. As observed from Table 3.5, the computed hole mobility of the ZB compounds is much higher than that of the WZ compounds, which is attributed to the significant difference in their effective mass resulting from their respective electronic dispersion of the valence band maxima (VBM) regime at the center of the Brillouin zone. This results in the difference in the respective relaxation times of the compounds. It is noteworthy that despite of large difference in carrier mobility, the relaxation time for both phases show small difference. This can be

attributed to the less discrepancy between their deformation potentials and elastic constants.

**Table 3.5. Calculated hole effective mass ($m_h^*$), deformation potential ($E_1$), elastic constant ($C_{ii}$), hole mobility (μ) and relaxation time (τ) of GaX compounds in ZB and WZ phases.**

| System | Phase | $m_h^*$ ($m_e$) | $E_1$ (eV) | $C_{ii}$ (GPa) | μ (m²/V.s) | τ (fs) |
|---|---|---|---|---|---|---|
| | | | | | | |
| **GaP** | ZB | 0.5 | 7.11 | 149.7 | 983 | 283 |
| | WZ | 0.62 | 7.47 | 180.3 | 628 | 224 |
| | | | | | | |
| **GaAs** | ZB | 0.47 | 6.66 | 123 | 1090 | 293 |
| | WZ | 0.64 | 7.09 | 152.1 | 544 | 200 |
| | | | | | | |
| **GaSb** | ZB | 0.39 | 6.6 | 91.4 | 1380 | 312 |
| | WZ | 0.58 | 7.1 | 118.5 | 543 | 181 |

After the computation of carrier relaxation time and relaxation time independent thermoelectric parameters like S, σ and $\kappa_e$ are evaluated and respective trends as a function of temperature are plotted in Figs. 3.6 and 3.7. As observed, the computed Seebeck co-efficient of GaP, GaAs and GaSb in ZB phase is 170, 176 and 126 μV/K at 300 K. It can be clearly observed that our computed value of Seebeck co-efficient for ZB GaAs is in excellent agreement with the prior experimental data (~ 170 μV/K),[59] which validates the calculation and supports the approach utilized, although the results of GaP and GaSb could not be compared with any experimental data due to their unavailability at same ambient conditions and carrier concentration. As far as trend is concerned, the Seebeck co-efficient for all three compounds increases linearly with temperature and attains a maximum value of about 328 and 345 μV/K at 1200 K for GaP in ZB and WZ phases, respectively. The electrical conductivity σ, (see Figs. 3.6(b) and 3.7(b)) shows significant difference in magnitudes with similar trend in both phases. It can be observed that the σ decreases exponentially with increase in

temperature. The temperature dependent variation of power factor ($S^2\sigma$) for ZB and WZ phases is shown in Figs. 3.6(c) and 3.7(c), respectively.

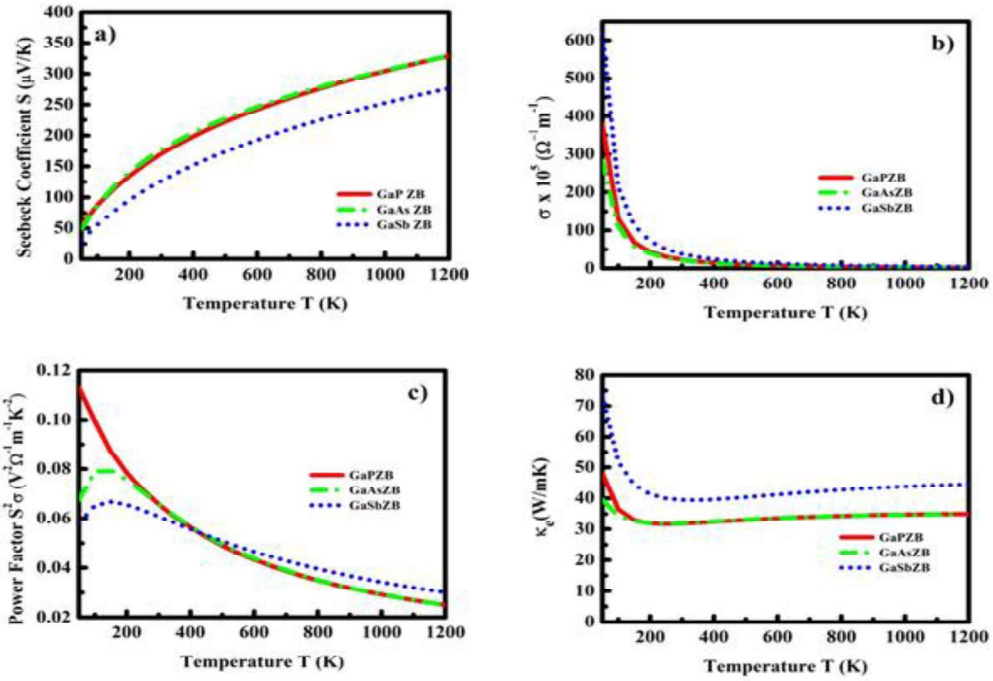


**Figure 3.6. Calculated temperature dependent electronic contributions to the thermoelectric properties of the GaX compounds in ZB phase: (a) Seebeck co-efficient, (b) electrical conductivity, (c) Power factor and (d) electronic contributions to thermal conductivity.**

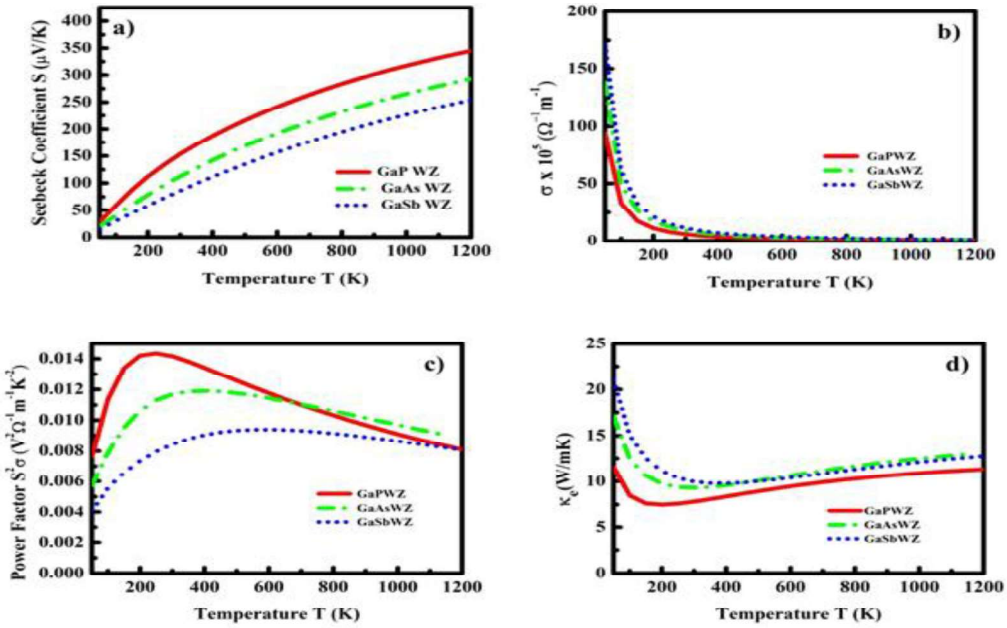


**Figure 3.7. Calculated temperature dependentelectronic contributions to the thermoelectric properties of the GaX compounds in WZ phase: (a) Seebeck co-efficient, (b) electrical conductivity, (c) Power factor and (d) electronic contributions to thermal conductivity.**

The room temperature values of power factor of GaP and GaAs in ZB phase is almost same (~0.065 $V^2\Omega^{-1}m^{-1}K^{-2}$) while, it is slightly lower (~0.060 $V^2\Omega^{-1}m^{-1}K^{-2}$) for GaSb. The Fig. 3.7(c) shows the trend of power factor as a function of temperature of GaX compounds in WZ phase, and it is noteworthy, that the magnitudes of all three compounds show significant difference of 0.014, 0.011 and 0.0084 $V^2\Omega^{-1}m^{-1}K^{-2}$at 300 K for GaP, GaAs and GaSb, respectively. The electronic thermal conductivity $\kappa_e$ (see Figs. 3.6(d) and 3.7(d)) shows reduction in low temperature regime (<200 K), after which it attains feeble enhancement with temperature and, at 1200 K, it attains the highest magnitude of 34.95, 34.78 and 44.52 W/mK and 11.32, 13.09 and 12.74 W/mK for GaP, GaAs and GaSb in ZB and WZ phases, respectively. The enhanced values of power factors and lower values of electronic conductivity $\kappa_e$ indicate the possibility of enhanced figure of merit ZT of these compounds if the thermal conductivity $\kappa_l$ is also found to be significantly low. After analyzing the electronic contributions to thermoelectric properties, we now turn our attention towards the underlying thermoelectric mechanism due to phonon contributions. For computing the phonon contribution to thermoelectric transport, the second order interatomic harmonic force constants (IFCs) generated under density functional perturbation approach (DFPT) approach[47] are utilized for further generating the third order IFCs. The phonon dependent thermoelectric parameters such as group velocity, mode Grüneisen parameters and scattering rate as a function of frequency are presented in Figure 3.8. As it can be observed from Figs. 3.8(a) and (d), the overall group velocity of the three acoustic modes attains higher magnitude for both phases of GaP with a dense accumulation in the case of WZ phase as the atomic contribution per unit cell is double

than that of the ZB polytype. This trend of group velocity is also validated from the nature of acoustic phonon modes in PDCs (see Fig. 3.3). The acoustic phonon branches are steeper in the case of ZB phase than that of WZ phase. As a consequence of this, the large deviation in frequency with respect to wave vector ***q*** is observed which is the measure of the group velocity. The volume dependent mode Grüneisen parameter (γ) which is the measure of anharmonicity arising due to phonon-phonon scattering

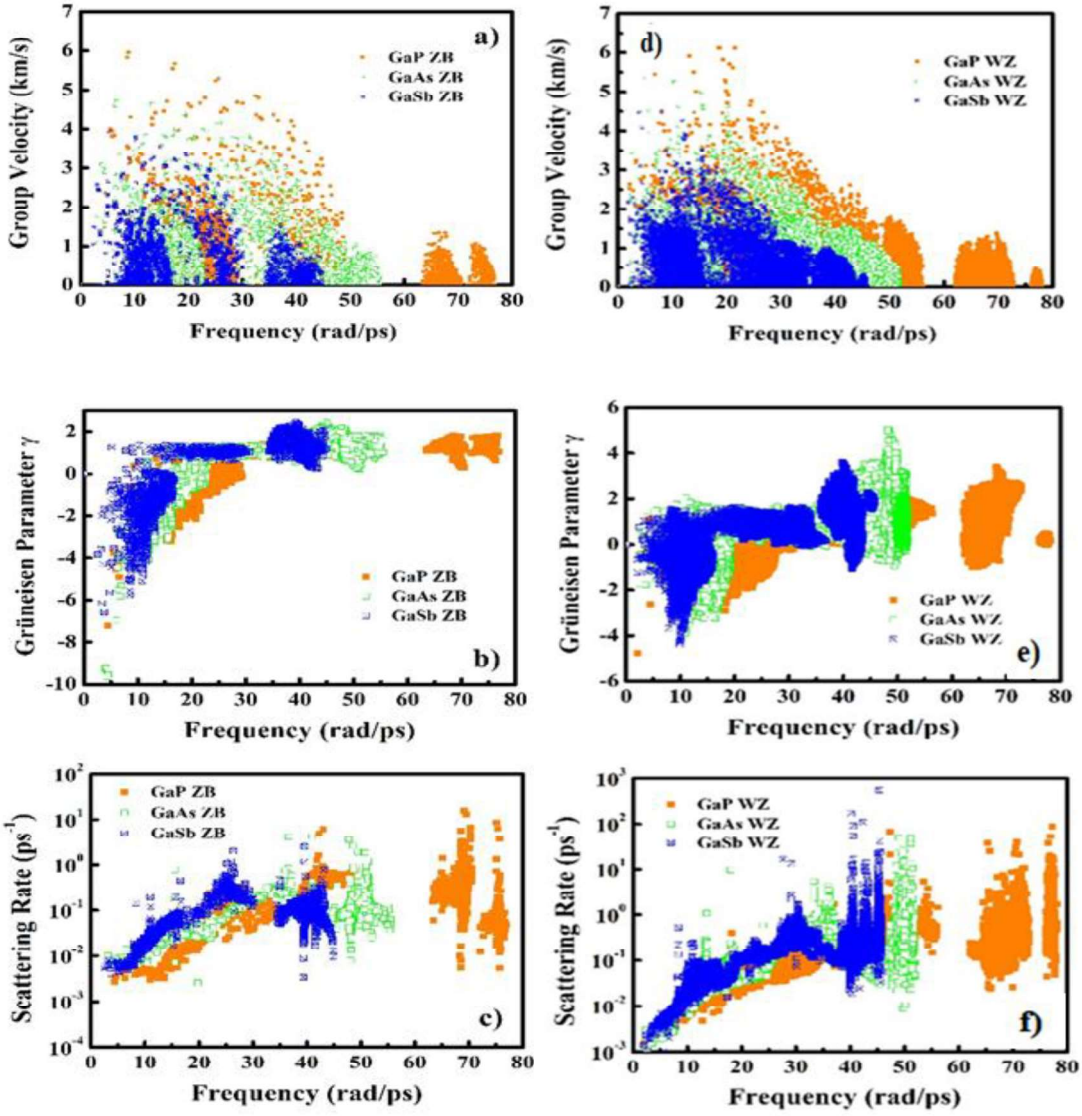


**Figure 3.8. Computed phonon dependent thermoelectric parameters (a, d) Phonon group velocity, (b, e) Mode Gruneisen parameters and (c, f) Phonon scattering rate for GaX compounds un ZB and WZ phases, respectively.**

mechanism is shown in Figs. 3.8(b) and (e) for ZB and WZ phases, respectively. The WZ phase attains higher magnitude of γ than the ZB phase revealing stronger phonon anharmonicity and reduced phonon lifetimes. The trend of reduction in phonon lifetimes can be observed explicitly from the scattering rates of GaX compounds. Figs. 3.8(c) and (f) present the phonon scattering rates as a function of phonon frequency. These plots reveal that the phonon-phonon scattering rates are higher for all WZ polytypes, and is highest for WZ GaP subjected to higher anisotropy between anion and cation masses. The comparison of the computed lattice thermal conductivity at 300 K with prior reported experimental and theoretical data is presented in Table 3.6. It can be observed that the computed lattice part of thermal conductivities is found in reasonable agreement with the prior reports,[60–65] except with one of the DFT based report[66] in which the isotope effect on thermal conductivity is considered. Moreover, it should be noted that the authors have performed the LDA based calculation for ZB compounds with inclusion of *d-orbital* electrons which might significantly affect the compound properties.[67]

The dramatic difference in magnitude of lattice conductivity as a function of temperature of GaX compounds due to phase variance can be clearly observed in Figs. 3.9(a) and (b). The magnitude of $\kappa_l$ is almost double for ZB GaP than WZ GaP pointing to the lower thermoelectric compatibility of ZB GaP; whereas, for GaAs and GaSb, the difference in $\kappa_l$ in both phases is comparable. Further, the inset of Fig. 3.9(a) represents the comparison of the present calculation and previously reported experimental and theoretical trends of thermal conductivity of GaX compounds in ZB phase. It is noteworthy that our computed values of thermal conductivity of GaX compounds

show good agreement with the prior reports for all GaX compounds in ZB phase; however, the slight difference in the magnitudes can be attributed to the isotope effects which were not included in the present calculation. The low temperature trends (< 300 K) of thermal conductivity reveal that the GaSb compound among the remaining two GaX compounds shows tremendous difference in the magnitude. We observe similar trend for WZ GaX compounds with crucial decrease in thermal conductivity especially observed for WZ GaSb (see Fig. 3.9(b)); these results predict signature contribution of WZ compounds in thermal management.

**Table 3.6. Lattice thermal conductivity ($\kappa_l$) at 300 K for GaX compounds in ZB and WZ phases.**

| System | Phase | Lattice Thermal Conductivity $\kappa_l$ ($Wm^{-1}K^{-1}$) at 300 K | | | | |
|---|---|---|---|---|---|---|
| | | **Present** | **Theory.[a]** | **Theory[b]** | **Theory[c]** | **Exp.[d]** |
| **GaP** | ZB | 83.87 | 77 | 123 | 72 | **100** |
| | WZ | 39.96 | - | - | - | **-** |
| **GaAs** | ZB | 39.91 | 45 | 52 | 55 | **45** |
| | WZ | 31.1 | - | - | - | **-** |
| **GaSb** | ZB | 22.75 | 36 | 42 | 33 | **40** |
| | WZ | 18.58 | - | - | - | **-** |

[a]Ref.[60] [Model]

[b]Ref.[66] [LDA]

[c,d]Ref.[68] [Model + Exp]

After computation of phonon contribution to thermoelectric properties, we assessed thermoelectric performance of these systems by computing the electronic and overall figure of merits $ZT_e$ and ZT. The variation in $ZT_e$ and ZT as a function of temperature is presented in Figs. 3.9 (c) and (e) and Figs. 3.9(d) and (f) for ZB and WZ phases, respectively. The trend of $ZT_e$ is similar for all ZB and WZ compounds (see Fig. 3.9(c) and (d)); whereas, in the case of magnitude, the GaP compound at 300 K possesses magnitude (~0.62 and 0.54) higher than GaAs (~0.61 and 0.37) and GaSb(~0.46 and

0.25) in ZB and WZ phases, respectively. The $ZT_e$ for both the phases show increase in magnitude with increase in temperature and after 800 K it almost show minor enhancement.

Finally, the overall figure of merit ZT as a function of temperature which is presented in Figs. 3.9(e) and (f) shows a linear increase with temperature for both phases. In

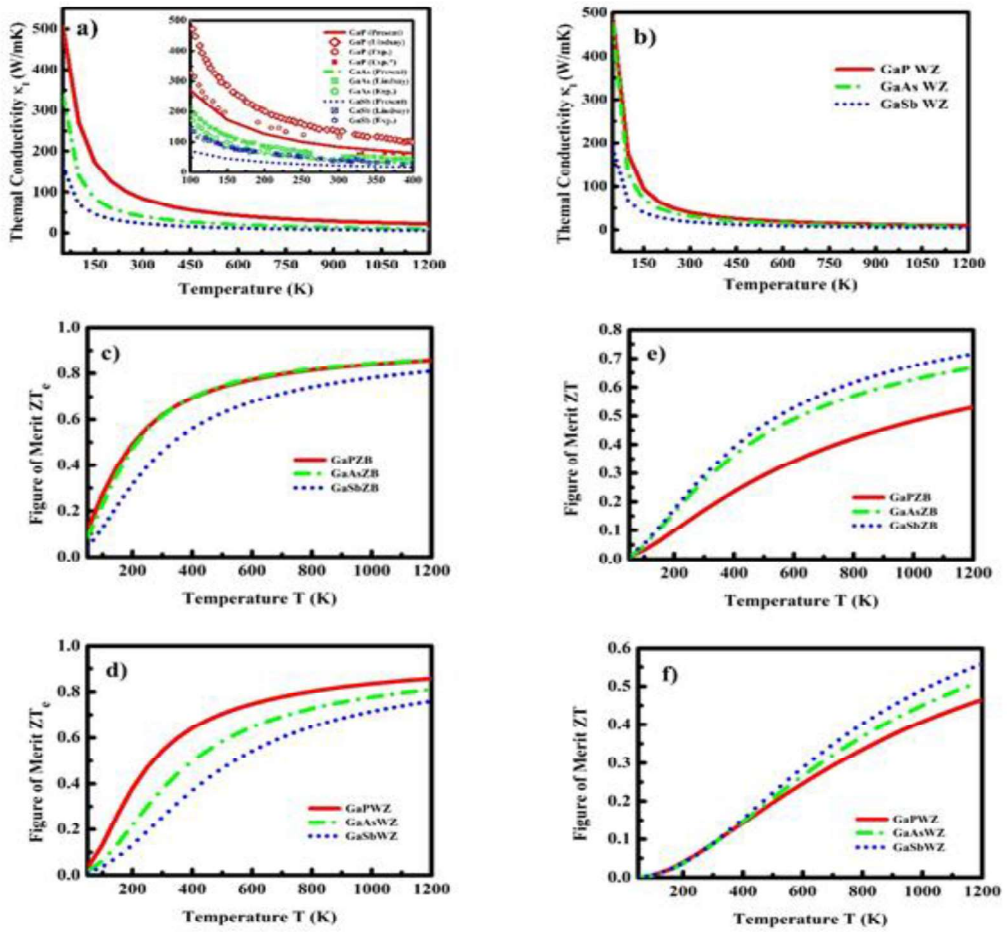


**Figure 3.9. Calculated thermoelectric parameters as a function of temperature (a, b) Thermal conductivity, (c, d) Electronic Figure of Merit and (e, f) Overall Figure of Merit for GaX compounds in ZB and WZ phases, respectively.**

addition, the Figs. 3.9(e) and (f) clearly show that the ZT is maximum for GaSb in both phases with magnitudes 0.29 and 0.088 at 300 K and, 0.72 and 0.56 at 1200 K in ZB and WZ phases, respectively. Our results show that the overall values of ZT is higher for

ZB phase. However, we expect that the nanostructured geometries of these compounds where, the WZ phase is more probable, may attain higher ZT value. Among all GaX compounds, GaSb is claimed to be more suitable for thermoelectric applications as it possesses highest figure of merit ZT and lowest thermal conductivity $\kappa_l$ with respect to other GaX compounds. Further, the higher value of ZT for all compounds in both phases at high temperature suggests that these compounds are suitable for high temperature thermoelectric devices.

### 3.3.2 Ground State Properties of GaX NWs

After assessing the phase dependent structural, electronic, vibrational, thermal and thermoelectric properties of GaX compounds, the WZ phase being more stable under confined conditions has been selected for calculating the ground state properties of the GaX compounds under two-dimensionally confined geometry; i.e. 1D NWs. The two-dimensional confined configurations of the GaX compounds, i.e. the WZ GaX NWs were constructed and optimized as per the description given in Section 3.2.2, and then were considered for further computation of the ground state structural, electronic and optical properties. To depict clear picture of the NW properties, the effect of size and external strain has been assessed by means of varying the diameter of the NWs and by imposing uniaxial compressive strain along the growth direction of the NWs. There are many reports on distinct III-V NWs showing importance of size and strain engineering,[69–71] thus providing clear insight to the carrier dependent modulation in the electronic transport properties. Most importantly, the III-V compounds are famous for their unique electronic band gap and markable carrier mobilities, that have made their immense utilization in the high frequency

nanodevices[1,2] and many other nanoelectronic devices,[36,72] the electro-optic properties of the same under nano dimensions have not gained appropriate attention. We in the proceeding sections describe the results of the calculated electro-optic transport properties of the GaX NWs under ambient and modified environments.

#### 3.3.2.1 Structural Properties

The structural properties of the GaX NWs are calculated after successfully optimizing the necessary parameters keeping the threshold criteria as mentioned in section 3.2.2. For direct assessment of the size dependent properties, the GaX NWs with three different diameters (~1, 2 and 3 nm) are constructed and studied, and within the next sections will be referred as GaP1, GaP2, GaP3, etc., indicating GaP NW with diameter approximately ~ 1, 2 and 3 nm, and so on. The well-defined optimized crystal structures of the GaX NWs with WZ phase can be observed in Figs. 3.10, 3.11 and 3.12 for GaP, GaAs and GaSb NWs, respectively. The top views of the NWs clearly indicate relaxed positions of the cations and anions residing at the equilibrium positions in the radial directions in contrast to the geometries observed in case of InAs NWs.[69] The reason for passivating surfaces of the GaX NWs with pseudo hydrogen is to remove surface dangling bonds and stabilize the crystal structure of the NWs by balancing Coulomb forces between the atomic species. It has been suggested, to passivate the NWs, as the surface dangling bonds are solely responsible for the false or pseudo electronic states near the band extrema and thus passivating the surface helps in better accurate prediction of the electronic dispersion curves.[73]

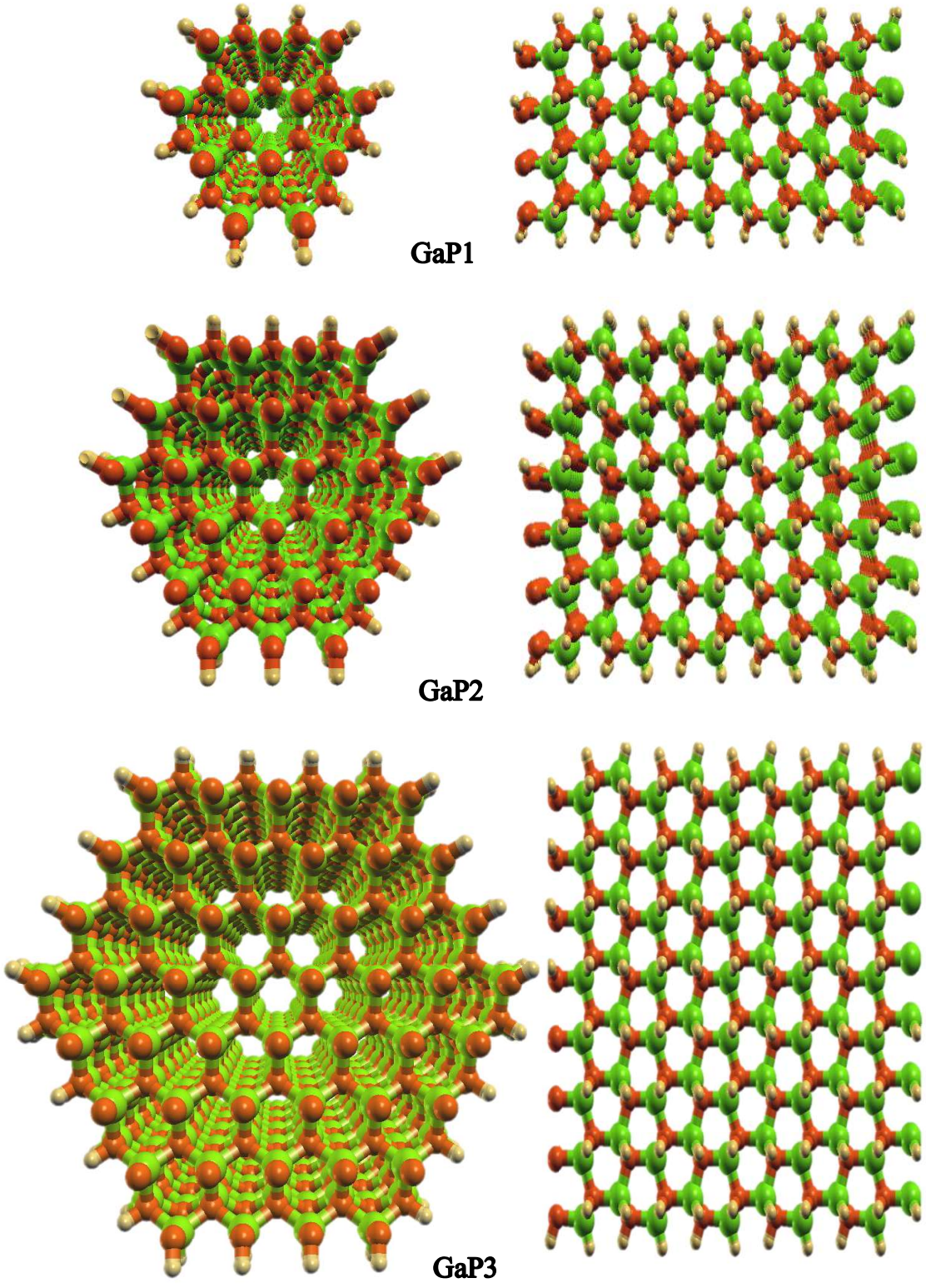


**Figure 3.10. Optimized top and side views of hydrogen passivated gallium phosphide nanowires (GaP NWs) with diameters ~ 1 (GaP1), 2 (GaP2) and 3 (GaP3) nm. (Spheres in green, orange and mustered yellow represent atoms of gallium, phosphorous and hydrogen, respectively.)**

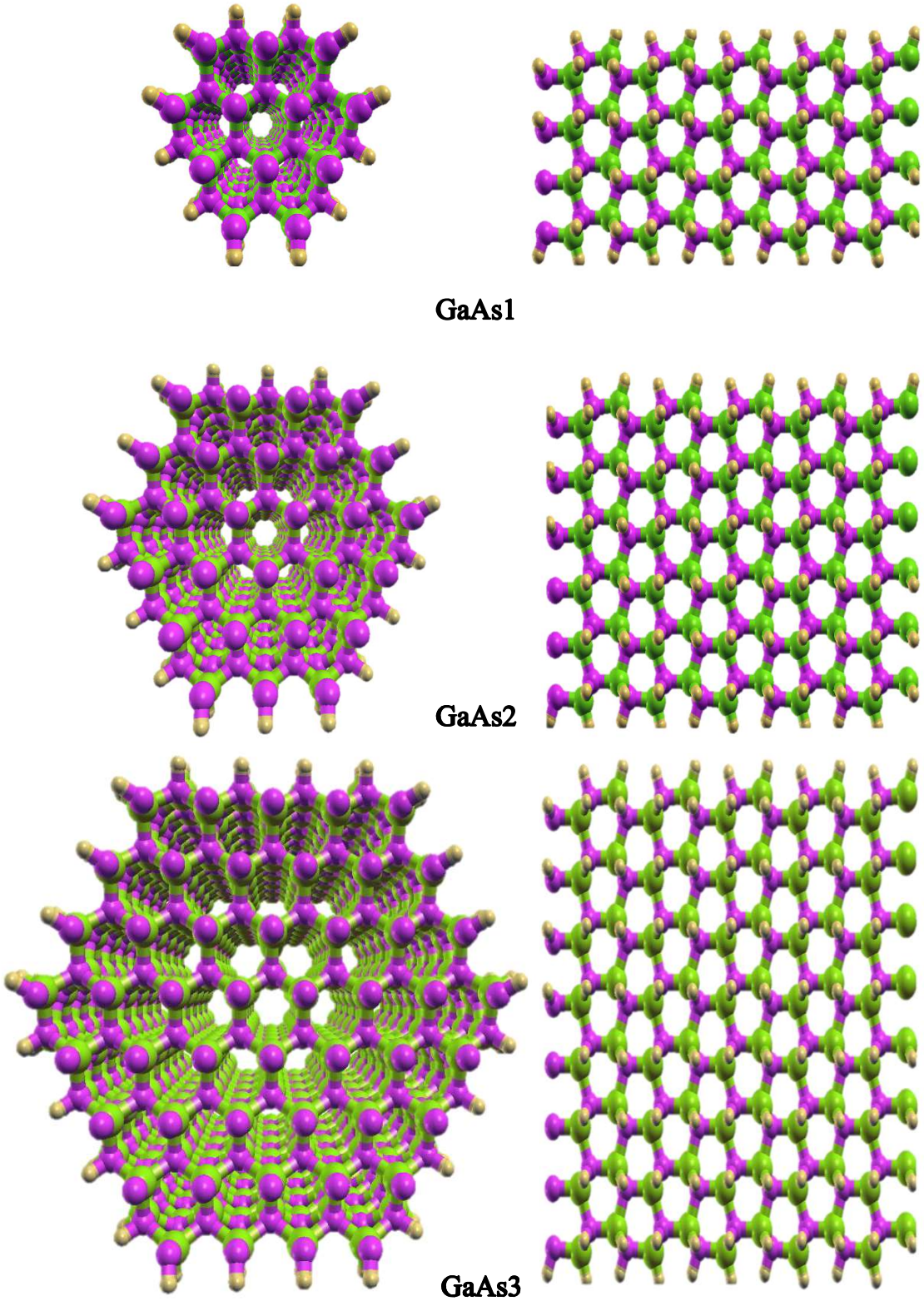


**Figure 3.11. Optimized top and side views of hydrogen passivated gallium arsenide nanowires (GaAs NWs) with diameters ~ 1 (GaAs1), 2 (GaAs2) and 3 (GaAs3) nm. (Spheres in green, purple and mustered yellow represent atoms of gallium, arsenic and hydrogen, respectively.)**

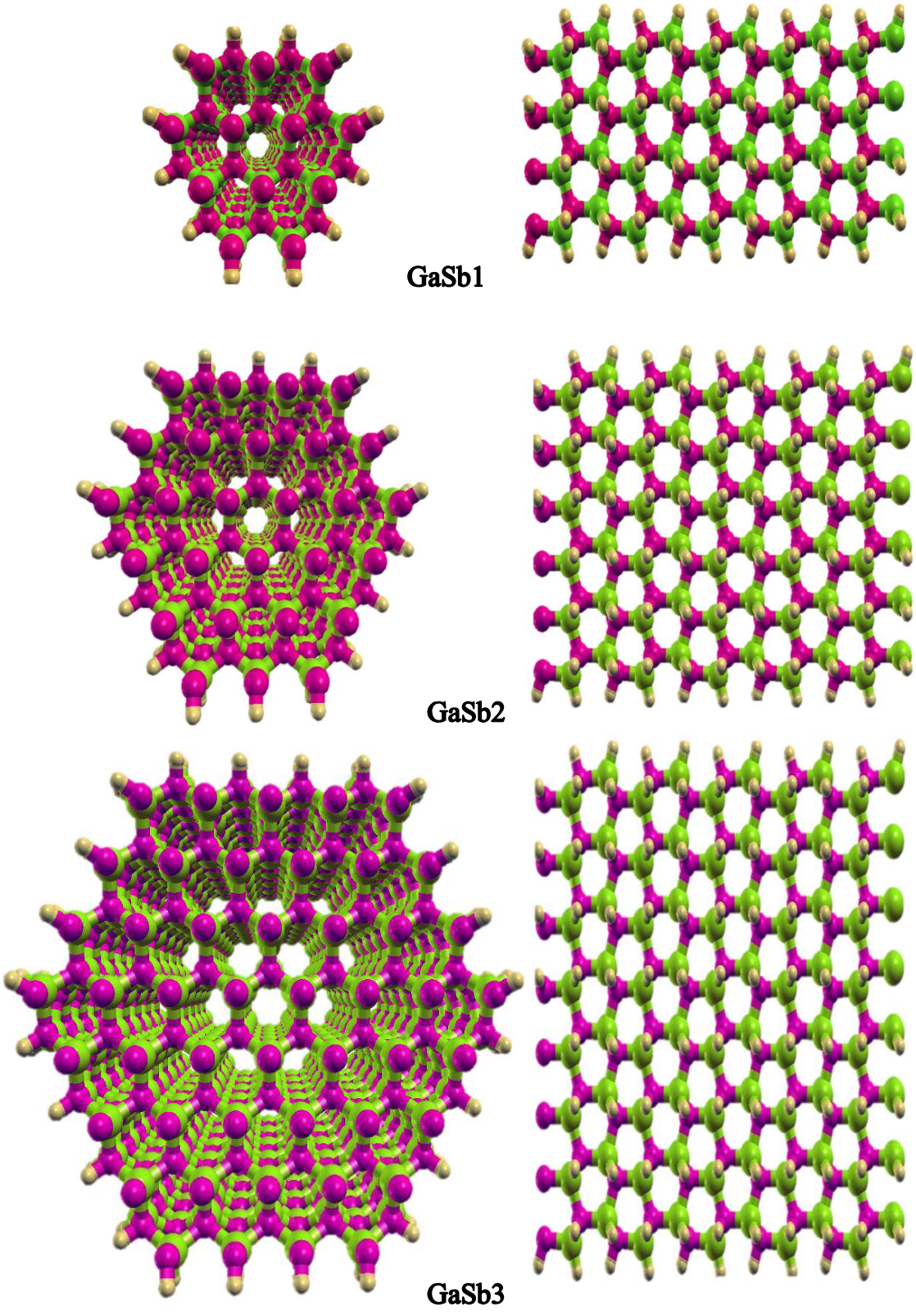


**Figure 3.12. Optimized top and side views of hydrogen passivated gallium antimonide nanowires (GaSb NWs) with diameters ~ 1 (GaSb1), 2 (GaSb2) and 3 (GaSb3) nm. (Spheres in green, pink and mustered yellow represent atoms of gallium, antimony and hydrogen, respectively.)**

Further, for confirming the structural stability of the NWs, energy of formation of the NWs is computed under size and strain modulating environments. The optimized structural parameters of the NWs with respective formation energies are presented in Table 3.7, and the energy of formation of the NWs as a function of diameter and strain is depicted in Fig. 3.13. As it can be observed from the Table 3.7, the lattice parameter shows enhancement subjected to the modification in anion radii, as in case of the bulk counterpart. The computed formation energy of all NWs is found to be negative implying towards the exothermic formation of NWs with stable configuration. Furthermore, the decrease in the NW formation energy as a function of NW diameter as shown in Fig. 3.13 (a) replicates the bulk like behavior of the NWs on increasing the diameter. Similar to the diameter dependent assessment of the NW stability, the modification in the NW stability on imposition of uniaxial compressive strain has been also assessed by computing energy of formation (see Fig. 3.13(b)). As expected, the increase in the uniaxial compressive strain causes decrease in energy of formation; however, the reduction is observed to be very feeble, which replicates that the

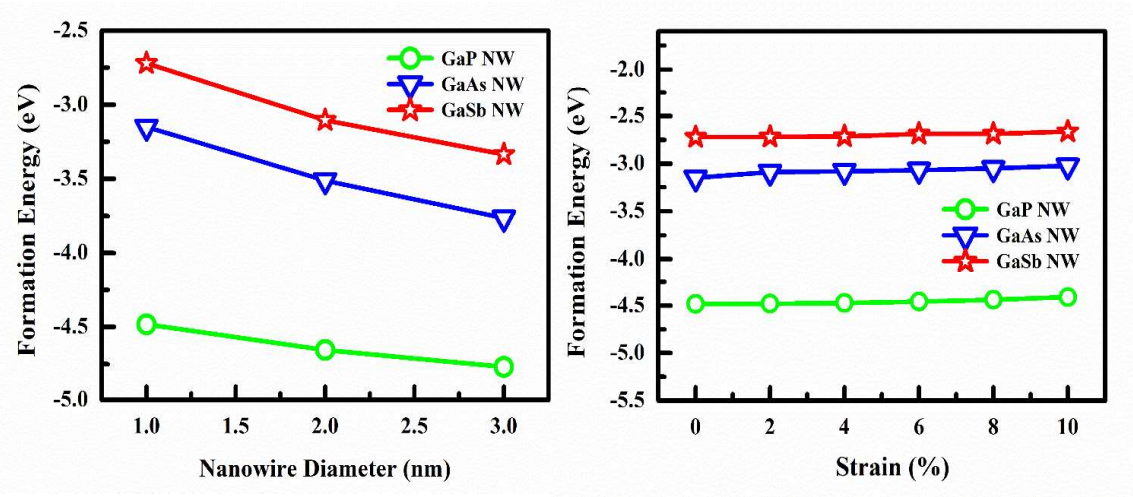


**Figure 3.13. Computed formation energy of GaX (X=P/As/Sb) NWs as a function of (a) NW diameter and (b) uniaxial compressive strain.**

structural stability of the NWs on imposition of compressive strain is not compromised, and lies within the permissible range so as to maintain structural configuration same as that of ambient conditions.

**Table 3.7. The structural and electronic properties of GaX (X=P, As, Sb) nanowires for three different diameters.**

| Property | Nanowires with diameter ~ 1, 2 and 3 nm | | | | | | | | |
|---|---|---|---|---|---|---|---|---|---|
| | GaP1 | GaP2 | GaP3 | GaAs1 | GaAs2 | GaAs3 | GaSb1 | GaSb2 | GaSb3 |
| | | | | | | | | | |
| **c/a** | 0.239 | 0.189 | 0.137 | 0.243 | 0.196 | 0.143 | 0.253 | 0.205 | 0.15 |
| $E_{FORM}^{NW}$ | -4.482 | -4.655 | -4.769 | -3.149 | -3.511 | -3.764 | -2.721 | -3.105 | -3.335 |
| **CBM** | 1.093 | 4.075 | -0.143 | -0.647 | 0.175 | -0.170 | -0.996 | -0.102 | -0.462 |
| **VBM** | -1.491 | -1.944 | -2.051 | -2.925 | -1.692 | -1.775 | -2.684 | -1.360 | -1.461 |
| $E_{Fermi}^{NW}$ | -0.199 | 1.065 | -1.097 | -1.786 | -0.758 | -0.973 | -1.840 | -0.731 | -0.961 |
| $E_g$ | 2.581 | 2.131 | 1.905 | 2.278 | 1.868 | 1.605 | 1.688 | 1.258 | 0.999 |
| **Nature** | I | I | **D** | I | I | I | I | I | I |
| | | | | | | | | | |

### 3.3.2.2 Diameter and Strain Dependent Electronic Properties of the NWs

The electron transfer/sharing/redistribution is the basic and dominating mechanism controlling the electronic transport properties of the material that can be precisely tuned when subjected to chemical doping, confinement or strain.[69,71,74,75] For understanding the basic electronic transport through the GaX NWs, the electronic dispersion curves along the high-symmetry path of the irreducible Brillouin zone along the NW growth direction (Z → Γ), with the spatial distribution of the electronic density of states (DOS) as a function of NW diameter are computed and the corresponding results are depicted in Figs. 3.14, 3.15 and 3.16 for GaP, GaAs and GaSb NWs, respectively. On imposing two-dimensional confinement, the electronic dispersion shows dramatic enhancement in the gap with modified curvature of the edge states. It is observed that the nature of the electronic bandgap for GaX NWs is found indirect in contrast to the respective bulk counterparts, except for the case of

GaP NW, in which on increasing the NW diameter to ~ 3 nm, the bandgap turns direct that was indirect in case of its bulk phases and low diameter NWs GaP1 and GaP2.

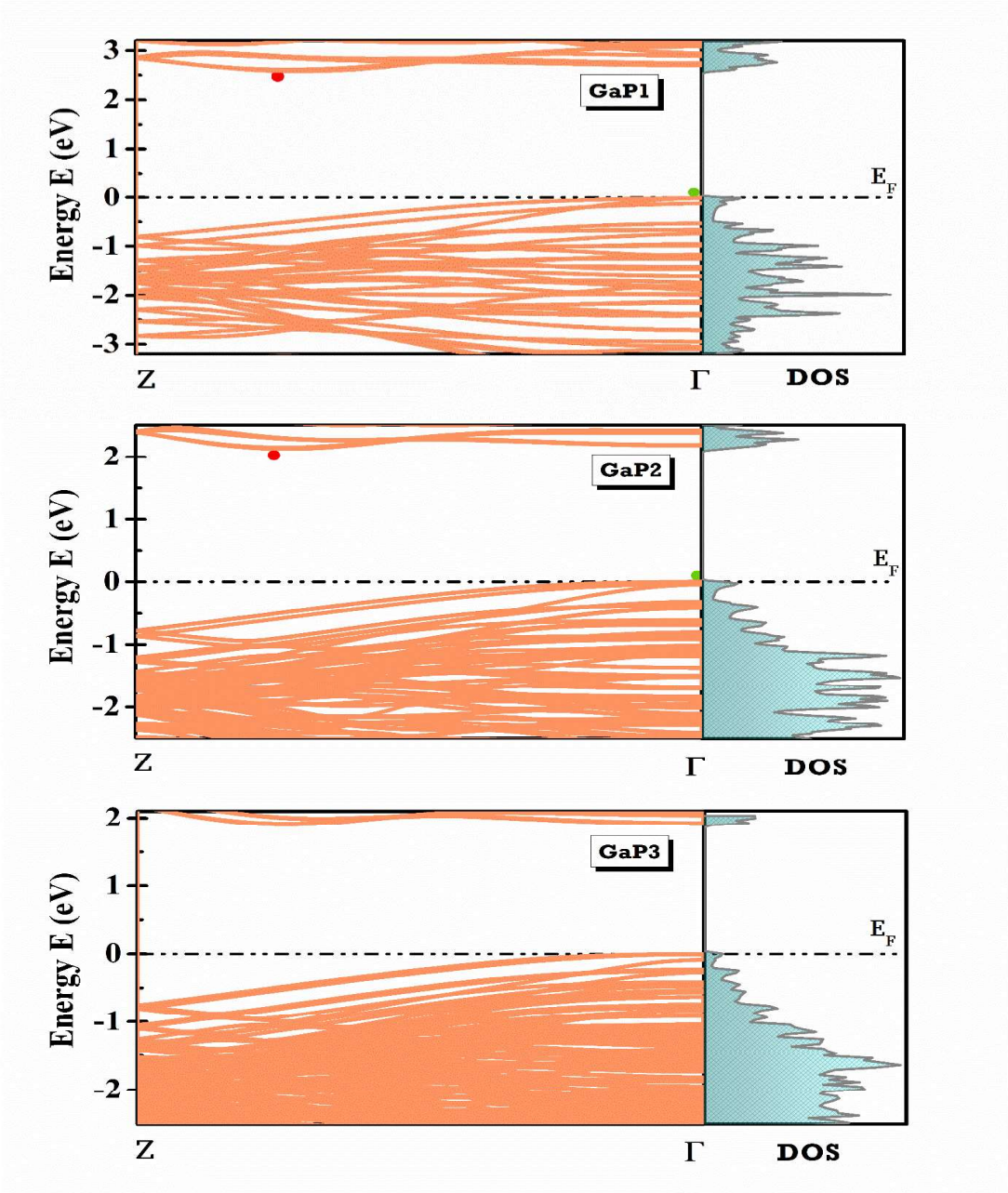


**Figure 3.14. Modulation in electronic band structure of GaP NWs subjected to change in NW diameter.**

With reference to the GaAs NW, the electronic nature does not agree with the result documented by Copple et al,[70] which reports indirect-direct bandgap transition (Γ →

X) in GaAs NW for diameter ~ 3 nm. The root cause of this difference could be the anisotropic nature of the NW and exclusion of the *d-orbital* electrons from the pseudopotentials utilized for calculation. Further, it is noteworthy that the nature and magnitude of the electronic bandgap is significantly modified due to variation in NW

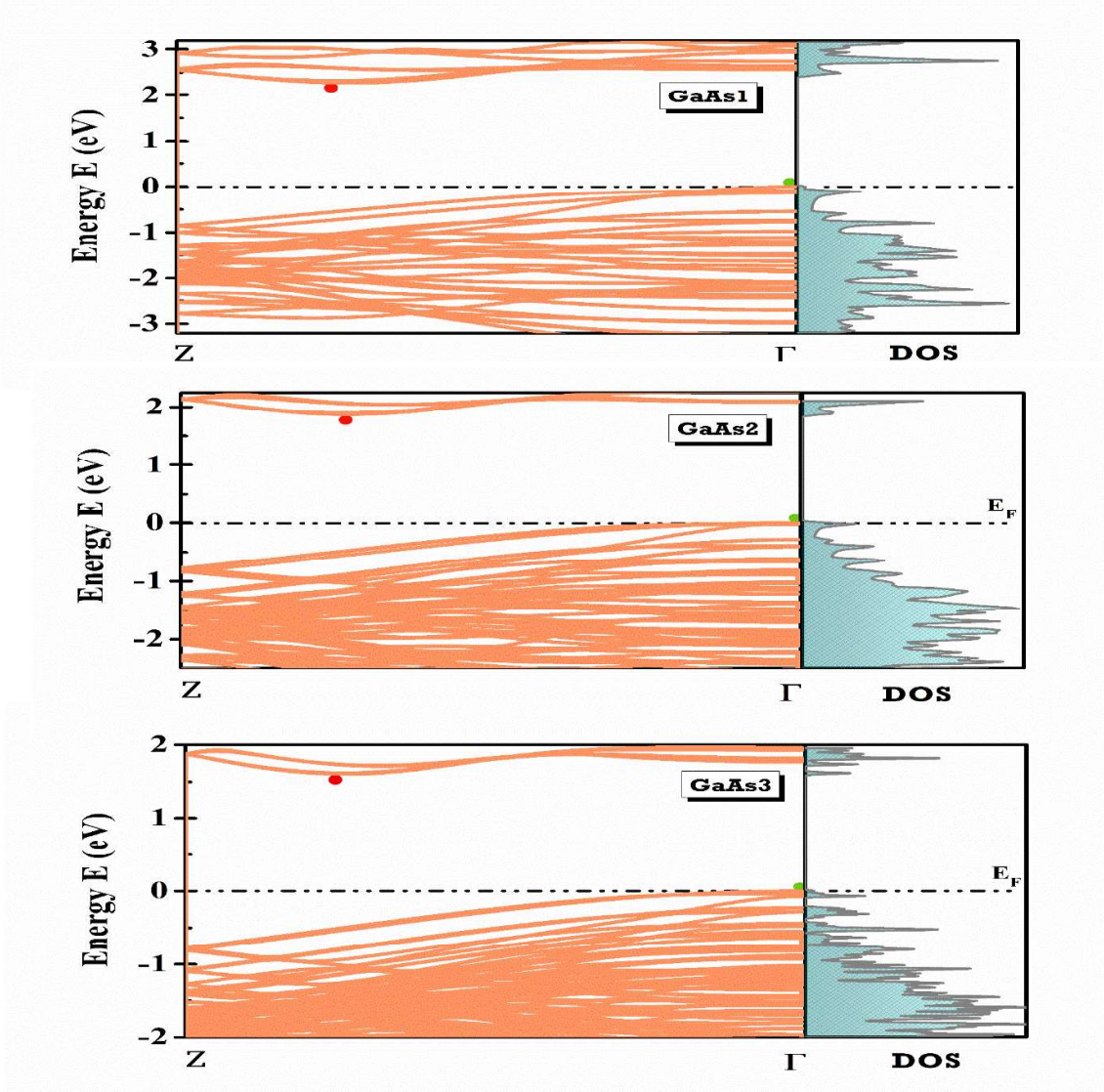


**Figure 3.15. Modulation in electronic band structure of GaAs NW subjected to change in diameter.**

dimensions showing effect of quantum confinement. Our computed bandgap value for GaAs NWs with diameters ~1, 2 and 3 nm are 2.27, 1.86 and 1.60 eV, respectively that are in good agreement with the experimentally measured values for higher

diameters which lie in the range 1.45-1.56 eV.[18,76] In case of the GaSb NWs, the bandgap reduces from 1.688 eV to 1.258 eV to 0.999 eV, as we move towards GaSb2

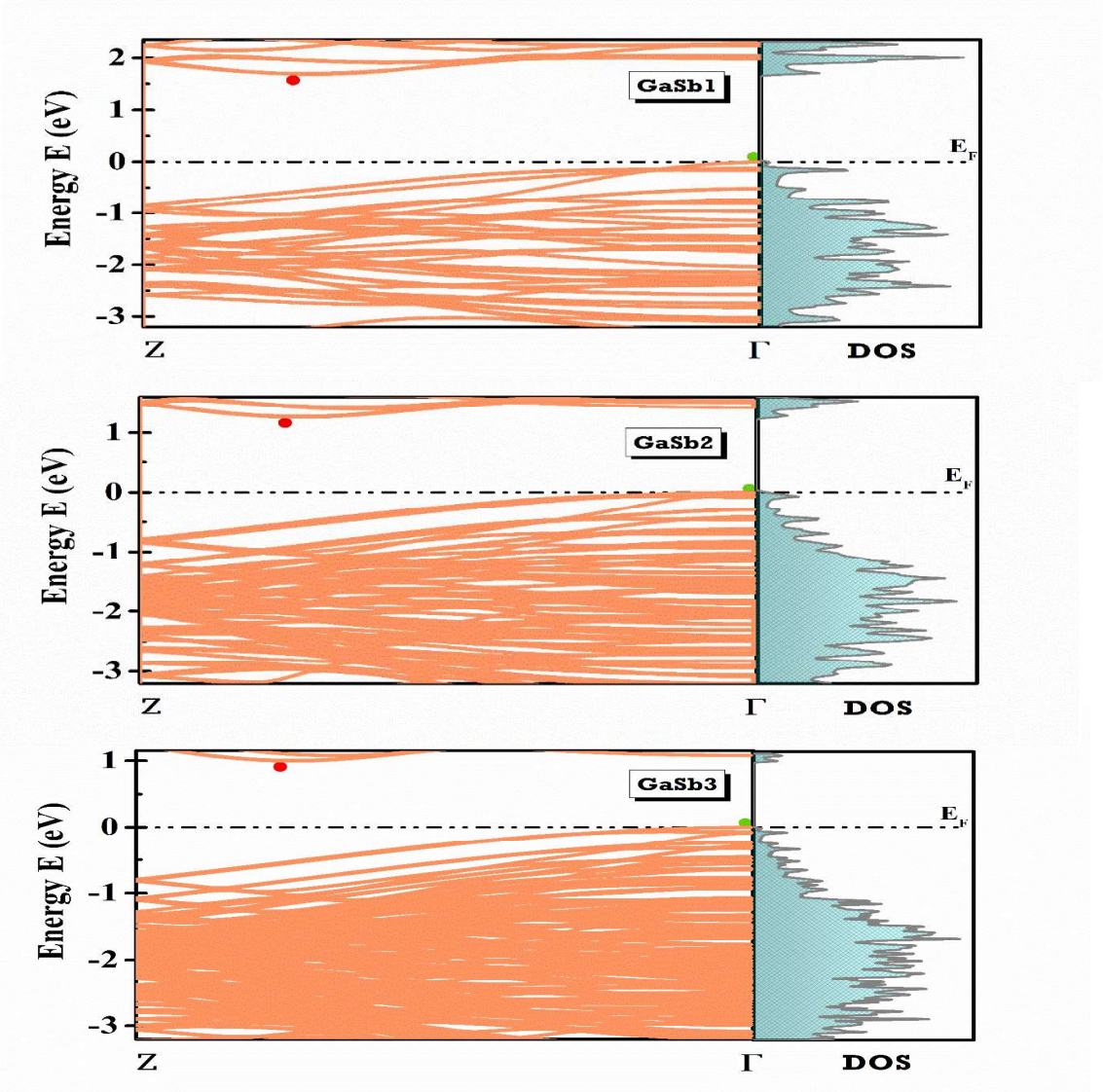


**Figure 3.16. Modulation in electronic band structure of GaSb NW subjected to change in diameter.**

and GaSb3. It is evident form the trends that as the diameter further gets increased, the NWs are likely to behave more like their bulk counterparts. The DOS plots of all NWs show spatially aligned van Hove singularities that are the signature of the two-dimensionally confined geometry of the NWs, and is responsible for NWs being more advantageous over their enhanced transport properties unlike the bulk counterparts.

The assessment of the size dependent electronic response of the GaX NWs conclude no change in the indirect nature of the electronic dispersion in case of GaAs and GaSb NWs; however, the bandgap magnitude shows markable reduction as a result of quantum size effect that is observed for all GaX NWs. Followed by the computation of the size (diameter) dependent electronic profiles of the GaX NWs, we further computed the electronic properties of the NWs as a function of uniaxial compressive strain for exploring the probability of tailoring the gap nature and thereby, the electro-optic transport. The reason for imposing uniaxial compressive strain lies within the factual unique one degree of freedom that is, the 0001 direction of the NWs, along which the NWs are grown. It is noteworthy, that the NWs are the unique 1D nanostructures, that are found more versatile than other nanostructures, due to their special ability to release/balance strain in the lateral directions making growth of the NWs possible on substrate materials possessing large lattice mismatch with the NWs.[77,78] The structural and electronic parameters of GaX1 NWs under the effect of external uniaxial compressive strain are listed in Table 3.8, and corresponding electronic dispersion curves are presented in Figs. 3.17, 3.18 and 3.19 for GaP1, GaAs1 and GaSb1 NWs, respectively. As it can be observed from the electronic dispersions, there is a makeable modulation in the magnitude and the nature of the bandgap under the effect of uniaxial compressive strain. The bandgap is found to get transformed from indirect to direct with the application of external strain with magnitude 4% for GaAs1 and GaSb1 NWs and 2% for GaP1 NW (see Fig. 3.17). The magnitude of uniaxial compressive strain was further increased up to 10%, that resulted in

monotonous reduction in bandgap for all NWs indicating enhancement towards the metallic character of the systems.

**Table 3.8. The structural and electronic parameters of GaP1, GaAs1 and GaSb1 NWs under the effect of uniaxial compressive strain.**

| System | Parameter | Uniaxial Compressive Strain (%) | | | | | |
|---|---|---|---|---|---|---|---|
| | | 0 | 2 | 4 | 6 | 8 | 10 |
| GaP1 | c/a | 0.239 | 0.234 | 0.229 | 0.224 | 0.219 | 0.215 |
| | $E_{FORM}^{NW}$ (eV) | -4.482 | -4.479 | -4.471 | -4.458 | -4.438 | -4.410 |
| | $E_{Fermi}^{NW}$ (eV) | -0.199 | -1.621 | -1.516 | -1.412 | -1.373 | -1.352 |
| | $E_g$ (eV) | 2.579 | 2.506 | 2.275 | 2.044 | 1.807 | 1.639 |
| | Nature | Indirect | **Direct** | **Direct** | **Direct** | **Direct** | **Direct** |
| GaAs1 | c/a | 0.243 | 0.238 | 0.233 | 0.228 | 0.223 | 0.218 |
| | $E_{FORM}^{NW}$ (eV) | -3.149 | -3.088 | -3.081 | -3.068 | -3.049 | -3.023 |
| | $E_{Fermi}^{NW}$ (eV) | -1.78 | -1.72 | -1.60 | -1.50 | -1.43 | -1.41 |
| | $E_g$ (eV) | 2.27 | 2.30 | 2.12 | 1.87 | 1.57 | 1.28 |
| | Nature | Indirect | Indirect | **Direct** | **Direct** | **Direct** | **Direct** |
| GaSb1 | c/a | 0.253 | 0.248 | 0.243 | 0.238 | 0.233 | 0.228 |
| | $E_{FORM}^{NW}$ (eV) | -2.721 | -2.719 | -2.713 | -2.685 | -2.685 | -2.663 |
| | $E_{Fermi}^{NW}$ (eV) | -1.84 | -1.82 | -1.76 | -1.60 | -1.54 | -1.49 |
| | $E_g$ (eV) | 1.68 | 1.71 | 1.52 | 1.28 | 1.03 | 0.78 |
| | Nature | Indirect | Indirect | **Direct** | **Direct** | **Direct** | **Direct** |

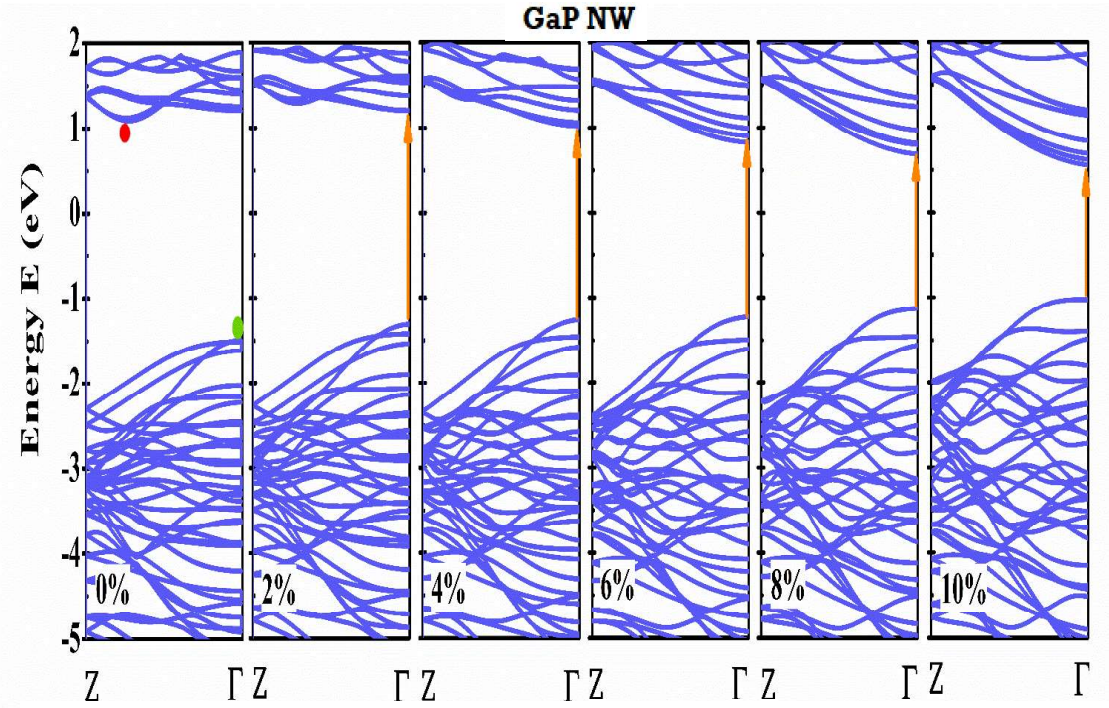


**Figure 3.17. Modulation in electronic band structure of GaP NW subjected to uniaxial compressive strain.**

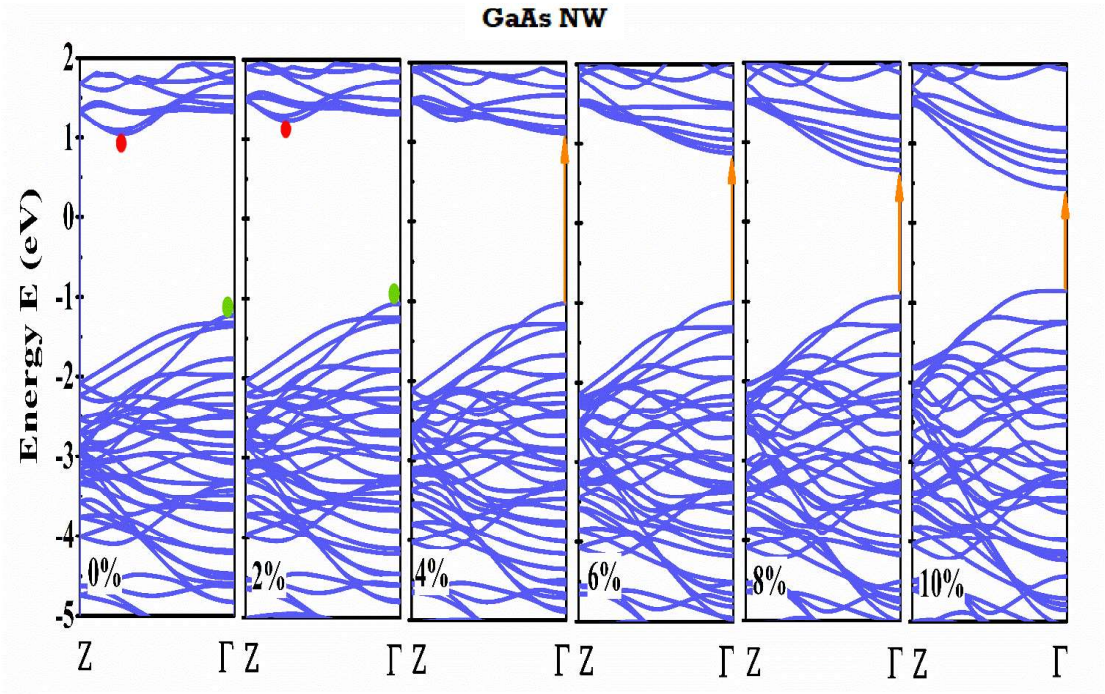


**Figure 3.18. Modulation in electronic band structure of GaAs NW subjected to uniaxial compressive strain.**

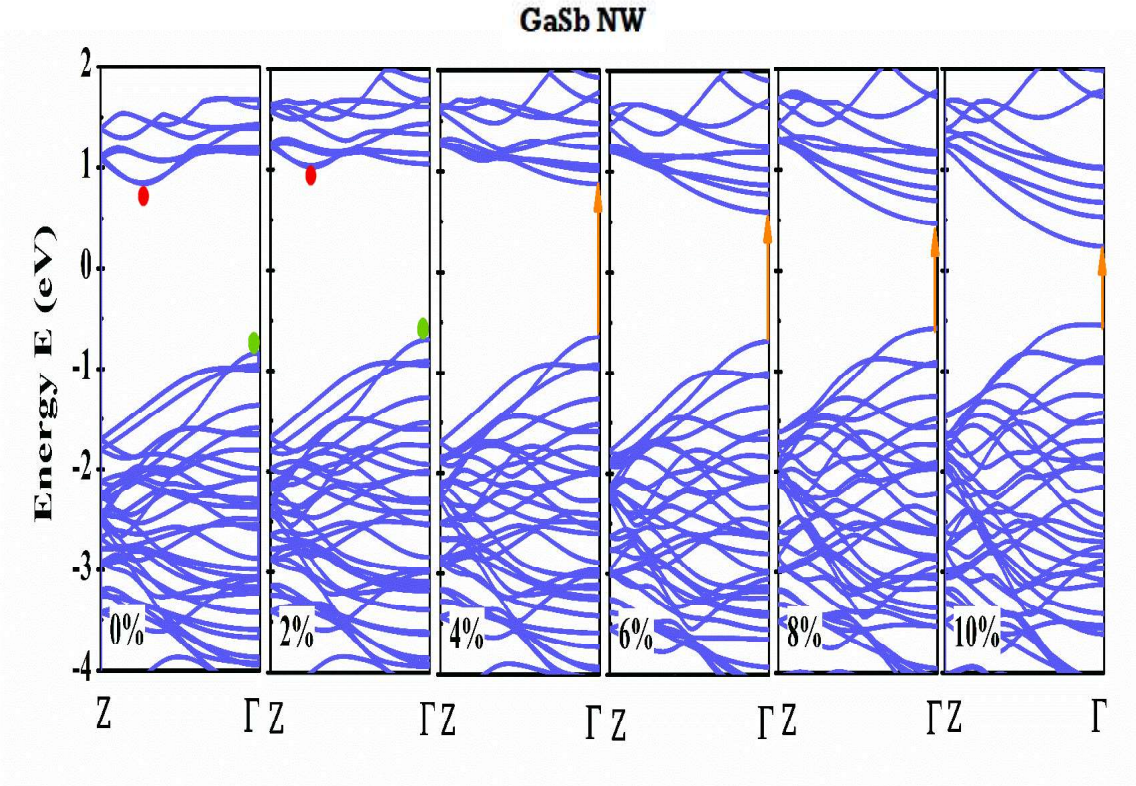


**Figure 3.19. Modulation in electronic band structure of GaSb NW subjected to uniaxial compressive strain.**

To get insight to the band edge re-alignment subjected to external strain, the conduction band minima (CBM) and valence band maxima (VBM) energies for the GaX1 NWs as a function of uniaxial compressive strain are plotted (see Fig. 3.20). The band-edge alignments of the GaX1 NWs with reference to strain also validate reduction in bandgap with modulation in the Fermi energy of the NWs.

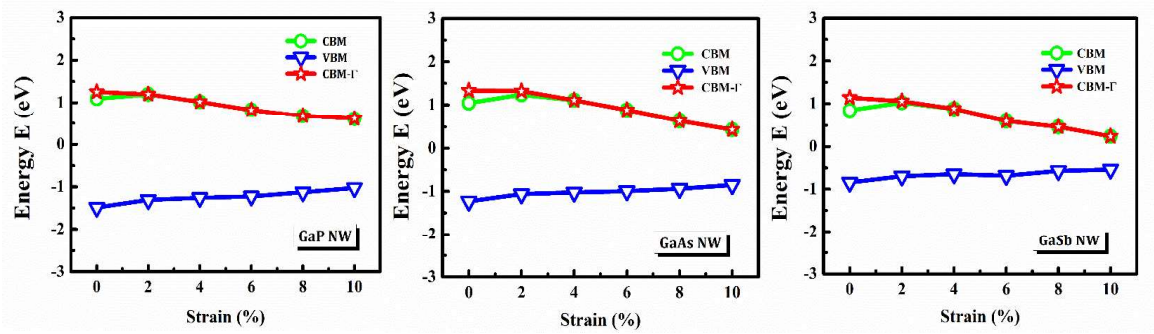


**Figure 3.20. Strain dependent electronic edge states (VBM/CBM) of GaP1, GaAs1 and GaSb1 NWs.**

### 3.3.2.3 Diameter and Strain Dependent Optical Properties of NWs

After understanding the electronic transport through the NWs, we now turn our attention towards the computation of the optical properties of the NWs. Similar to the electronic transport properties, the size and strain dependent optical profiles are also computed. The frequency dependent complex di-electric function ε(ω) as a function of photon energy utilized for further calculation of optical parameters like refractive index (η), loss function L(ω), reflectivity R and absorption co-efficient (α) is computed using the random phase approximation (RPA).[49,50] The optoelectronic devices such as optical LEDs, and photovoltaic solar cells the material should possess direct energy bandgap with the magnitude lying within the range of that of the optical electromagnetic spectral range (1.6-3.2 eV).

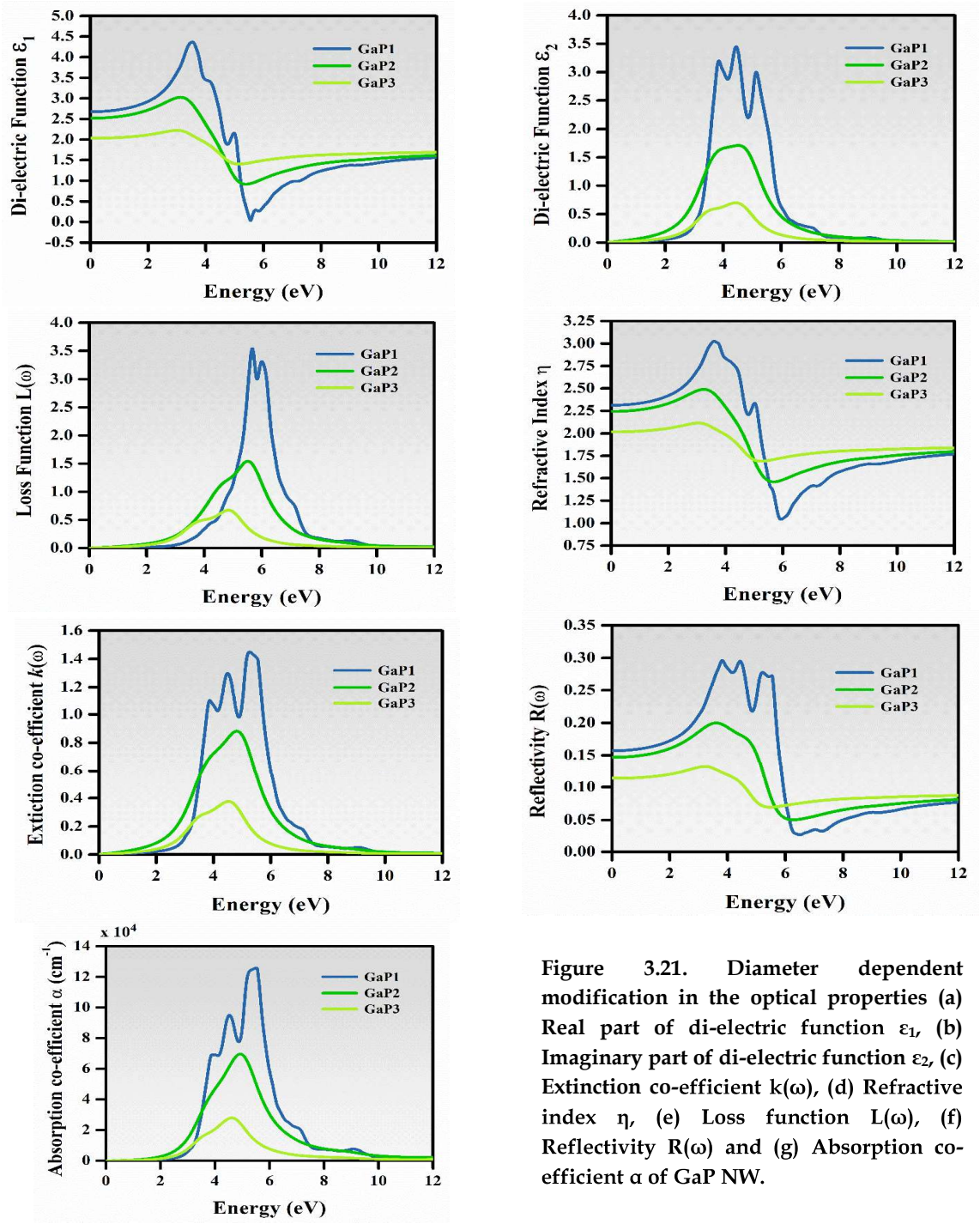


**Figure 3.21. Diameter dependent modification in the optical properties (a) Real part of di-electric function $\varepsilon_1$, (b) Imaginary part of di-electric function $\varepsilon_2$, (c) Extinction co-efficient k(ω), (d) Refractive index η, (e) Loss function L(ω), (f) Reflectivity R(ω) and (g) Absorption co-efficient α of GaP NW.**

Further, the electronic and optical bandgaps are alike if the bandgap is direct and vice-versa. In case of indirect semi-conductors, the optical bandgap can be estimated from the absorption profile or PL spectra. From the results of electronic properties of the NWs, we can observe that the bandgap for GaP, GaAs and GaSb NWs is within the

desirable range which provided motivation for further investigating their optical response. Moreover, the major application of III-V compounds is found in the field of optoelectronic and photovoltaic devices; hence, it is necessary to understand the optical transport of these NWs under modified conditions. Figs. 3.21, 3.22 and 3.23

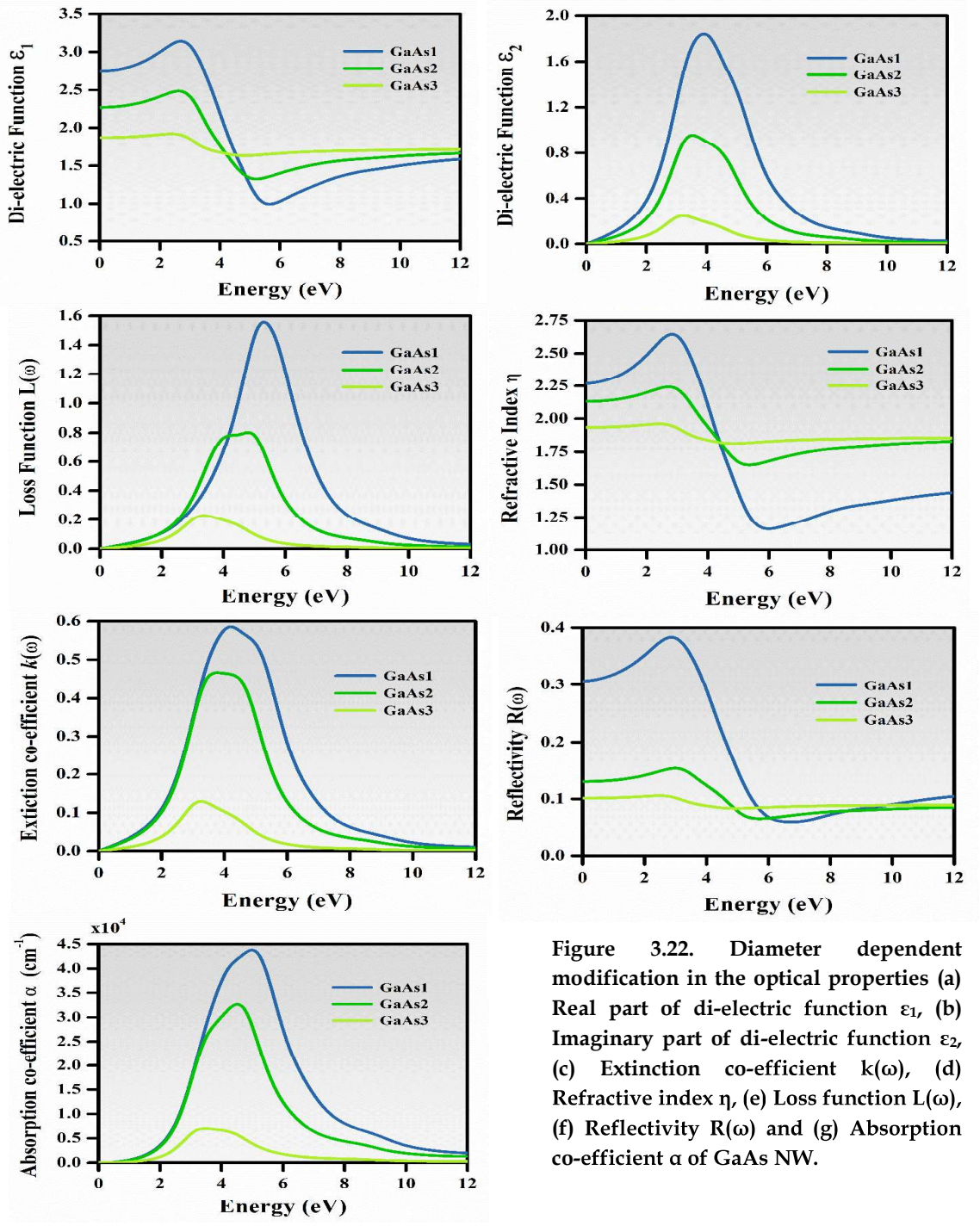


**Figure 3.22. Diameter dependent modification in the optical properties (a) Real part of di-electric function $\varepsilon_1$, (b) Imaginary part of di-electric function $\varepsilon_2$, (c) Extinction co-efficient k(ω), (d) Refractive index η, (e) Loss function L(ω), (f) Reflectivity R(ω) and (g) Absorption co-efficient α of GaAs NW.**

represent the diameter dependent optical properties like imaginary and real parts of complex di-electric function ε(ω), reflectivity, loss function L(ω), etc., for GaP, GaAs and GaSb NWs, respectively.

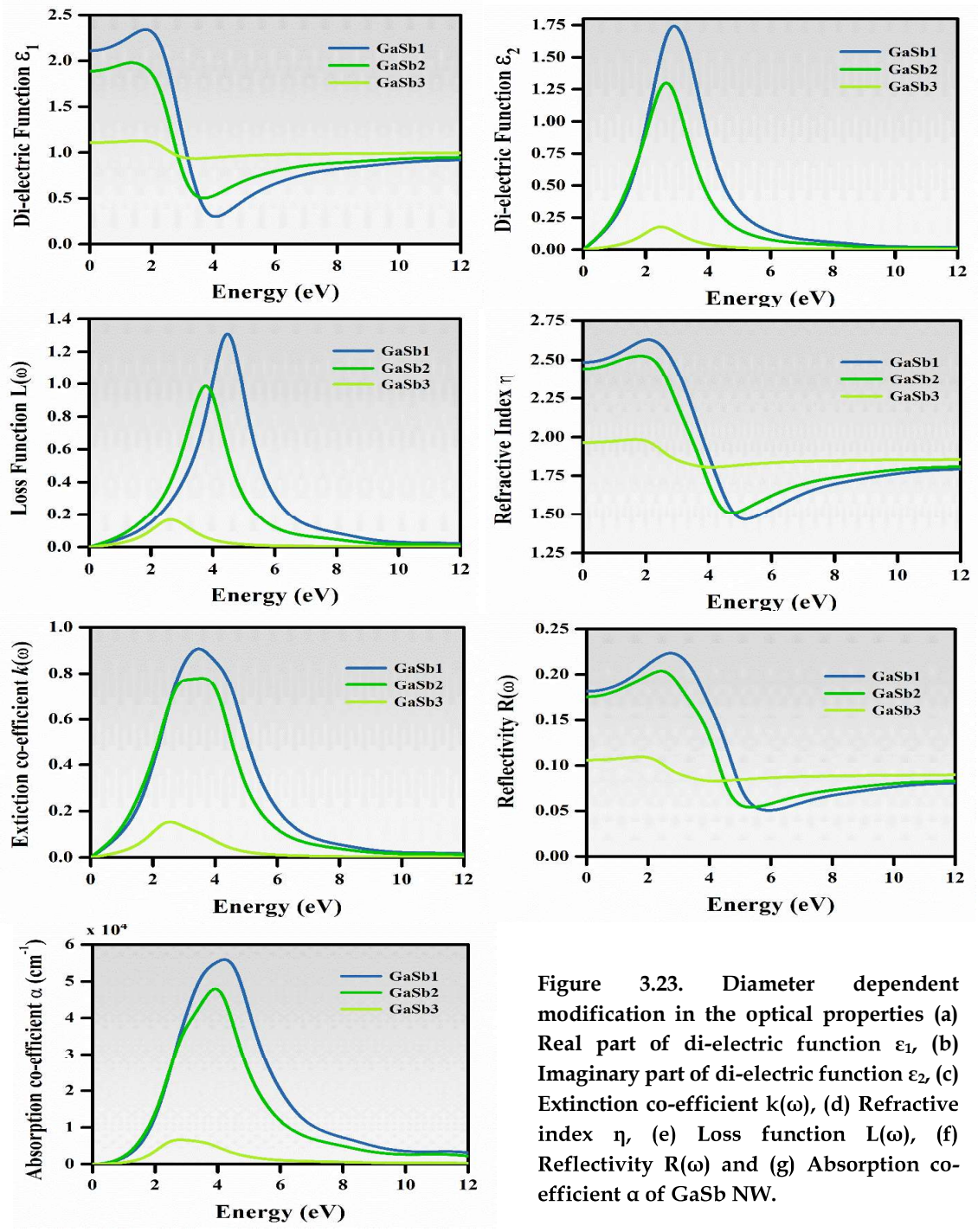


**Figure 3.23. Diameter dependent modification in the optical properties (a) Real part of di-electric function $\varepsilon_1$, (b) Imaginary part of di-electric function $\varepsilon_2$, (c) Extinction co-efficient k(ω), (d) Refractive index η, (e) Loss function L(ω), (f) Reflectivity R(ω) and (g) Absorption co-efficient α of GaSb NW.**

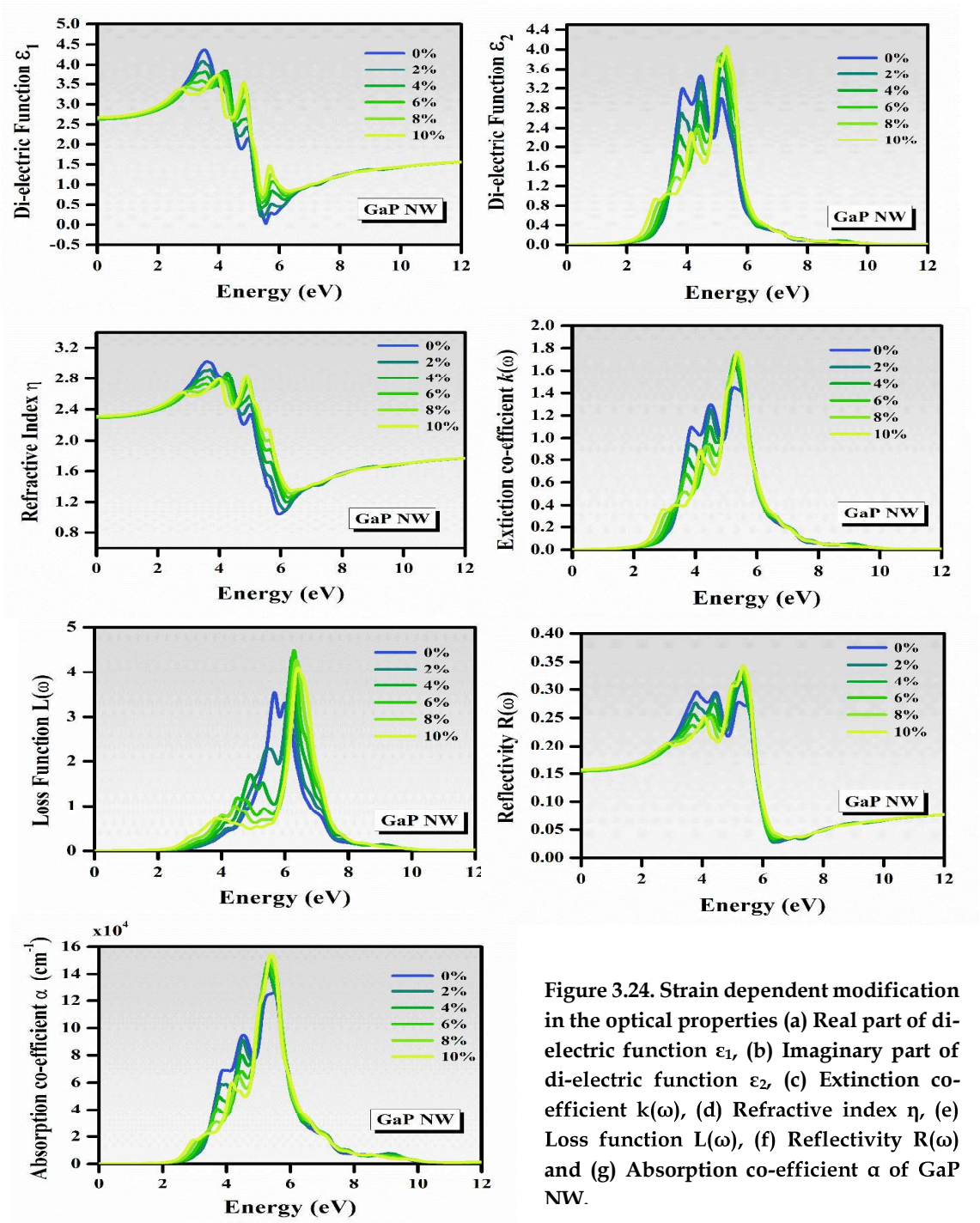


**Figure 3.24. Strain dependent modification in the optical properties (a) Real part of di-electric function $\varepsilon_1$, (b) Imaginary part of di-electric function $\varepsilon_2$, (c) Extinction co-efficient k(ω), (d) Refractive index η, (e) Loss function L(ω), (f) Reflectivity R(ω) and (g) Absorption co-efficient α of GaP NW.**

As it can be observed clearly, there is dramatic modulation in the real and imaginary components of the complex di-electric function in all three NWs. The sharp peak emerging in the imaginary part of the di-electric function plots in all cases indicates strong quantum confinement arising from size reduction. It should be noted, increase

in NW diameter causes reduction in the peak intensity, and enhancement in FWHM of the spectra. The absorption characteristics of any material can be predicted from the trends of the imaginary part of the complex di-electric function. In the present case, it can be observed that the origin of the absorption spectra (see Figs. 3.21, 3.22 and 3.23) occurs around 2 eV, which validates their utilization in the optoelectronic devices.

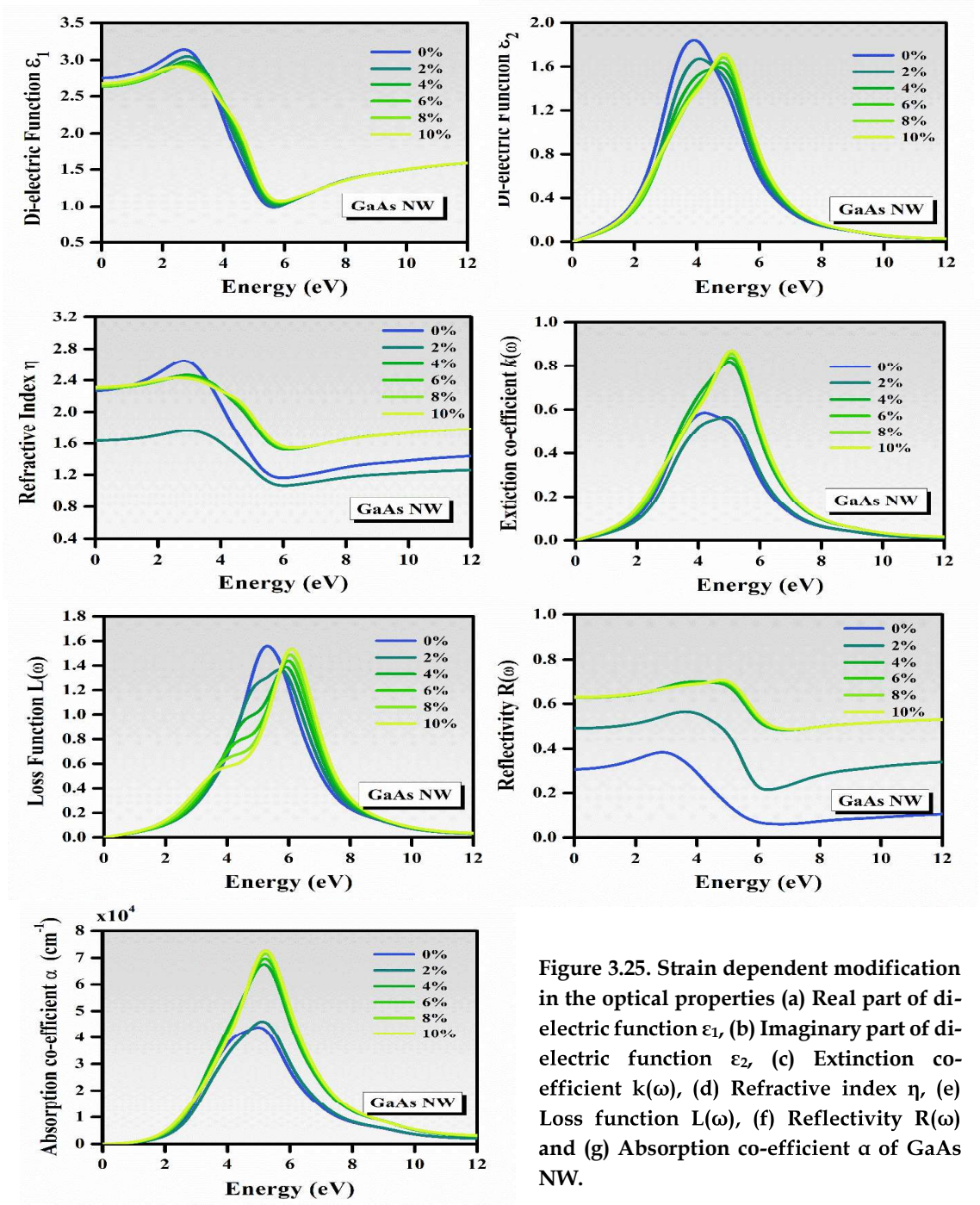


**Figure 3.25. Strain dependent modification in the optical properties (a) Real part of di-electric function $\varepsilon_1$, (b) Imaginary part of di-electric function $\varepsilon_2$, (c) Extinction co-efficient k(ω), (d) Refractive index η, (e) Loss function L(ω), (f) Reflectivity R(ω) and (g) Absorption co-efficient α of GaAs NW.**

Further, the strain dependent optical properties of the GaX1 NWs (see Figs. 3.24, 3.25 and 3.26 for GaP1, GaAs1 and GaSb1, respectively) show dramatic shift in the optical responses on imposition of compressive strain. The imaginary contributions to complex di-electric function which replicate the absorptive capacity of any material,

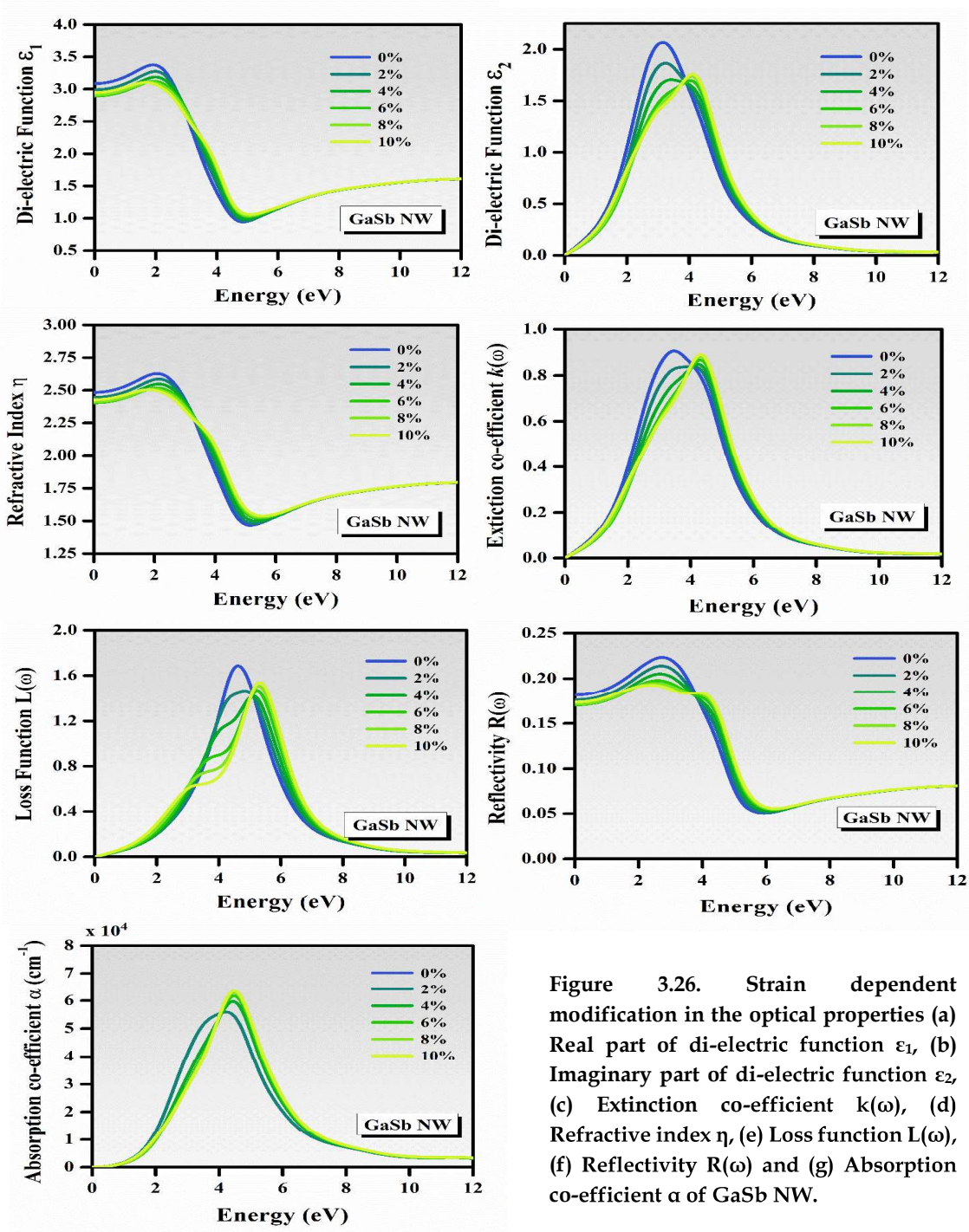


**Figure 3.26. Strain dependent modification in the optical properties (a) Real part of di-electric function $\varepsilon_1$, (b) Imaginary part of di-electric function $\varepsilon_2$, (c) Extinction co-efficient k(ω), (d) Refractive index η, (e) Loss function L(ω), (f) Reflectivity R(ω) and (g) Absorption co-efficient α of GaSb NW.**

in all three cases show markable red shift near the lower energy side of the frequency, indicating towards improved absorption within the visible regime (see Figs. 3.24, 3.25 and 3.26). The same can be confirmed from the computed absorption spectra of the GaX1 NWs. Interestingly, the shifts are observed as a consequence of indirect-to-direct bandgap transition, that suppresses the non-radiative transitions and promotes radiative transitions. Furthermore, the peak absorbance is observed near the extrema of the visible spectra for all three NWs which implicates that the NWs can be utilized for the large range of visible spectra covering the ultra-violet regime of the spectra too. In a nut-shell, both the size effect and the strain effects can be utilized for engineering the electro-optic profiles and convert non-radiative transitions to radiative transitions, and thus improvement in the overall efficiency of the material can be achieved.

## 3.4 Conclusion

Gallium pnictides GaX (X=P, As, Sb) being the novel III-V compounds have been systematically investigated for their structural, electronic, phonon, optical, thermal and thermoelectric properties using *state-of-art* density functional theory (DFT). The two distinct polytypic phases cubic zinc blende and hexagonal Wurtzite have been considered. The hexagonal Wurtzite phase is a consequence of dimensional confinement. The LDA predicted structural and electronic properties are in agreement with the reported experimental data with ~1.5% underestimation. The reason for such results is the over binding of atoms within the LDA based approach; however, it has been observed for various III-V compounds yielding better predictions of ground state properties as compared to the generalized gradient approximation (GGA).[52] It is observed that unlike GaP, GaAs and GaSb compounds possess direct electronic

bandgap with desirable bandgap in both phases. These two novel characteristics indicate their applicability in the optoelectronic and photovoltaic devices. Further, the validation of dynamical stability of these materials was done by computing phonon dispersion curves (PDCs) and phonon density of states (PHDOS), and absence of imaginary frequency and soft phonon modes suggest these compounds stable in both phases. Followed by dynamical stability, the thermal stability of the compounds was investigated by computing thermodynamic functions. The computed functions validate standard laws and trend thereby proving thermal compatibility of the compounds in both phases. After the confirmation of structural, dynamical and thermal stabilities of these compounds under both phases, their applicability as thermoelectric materials have been tested by means of computing temperature dependent thermoelectric parameters. The trends of computed Seebeck co-efficient, electrical conductivity and power factor, etc. are quite similar in both phases with significant differences in the magnitudes. In case of computed lattice thermal conductivity, the computed magnitudes in ZB phase agree well with the prior experimental reports, while the WZ phase remains incomparable owing to lack of experimental results under bulk phase. Further, apart from the markable power factor magnitude, the results on thermal conductivity also support GaSb to be more suitable for thermoelectric applications having lowest magnitude of lattice conductivity than other two GaX compounds with magnitudes 22.75 and 18.58 W/mK at 300 K in ZB and WZ phases respectively; however, these values are higher than the conventional materials used for thermoelectric applications. Further, the high-temperature (1200 K) thermal conductivities of GaP, GaAs and GaSb in ZB and WZ phases are 21.53, 9.99

and 5.8 W/mK and 9.53, 7.53 and 4.59 W/mK respectively, which suggest GaSb to be most suitable for high-temperature thermoelectric applications. After tip-to-toe investigations of GaX compounds under bulk phases, unique 1D NWs were constructed from the WZ bulk unit cells, and their ground state structural, electronic and optical properties were investigated under size and strain effects. The electronic dispersions of the NWs suggest decrease in gap on increasing NW diameter, and amongst all GaX NWs, the GaP NW stand out to be electronically transformed into a direct band gap semiconductor at ~ 3 nm diameter. On the other hand, the uniaxial compressive strain effect cause reduction in gap with electronic transition occurring at 2% strain for GaP1 NW, and 4% for the remaining two NWs. Following to this, from application point of view, the optical properties of the NWs were calculated to assess their applicability in the field of optoelectronics. The diameter and strain dependent results of optical properties suggest a pathway of getting tailor-made properties of the NWs. The frequency dependent responses of absorption co-efficient of all three NWs under the effect of change in diameter and strain clearly reveal the wide range of tunability of the absorption spectra ranging from visible to ultra-violet regime of the electro-magnetic spectrum. Also, from the electronic and optical profiles under size and strain effect, we can infer that tuning critical size and strain, non-radiative transitions can be converted to radiative transition, thus increase in overall efficiency of the material can be foreseen. Further, the well-optimized structural and ground state electro-optic properties of these NWs can be considered as a blueprint for the construction of heterostructured NW configurations, that not only help in controlling the carrier dynamics within the material but also provides a much better solution for

enhancing the efficiency of present energy applications based devices owing to their multi-purpose and versatile nature.

## References


(1) Baig, S. A.; Boland, J. L.; Damry, D. A.; Tan, H. H.; Jagadish, C.; Joyce, H. J.; Johnston, M. B. An Ultrafast Switchable Terahertz Polarization Modulator Based on III-V Semiconductor Nanowires. *Nano Lett.* **2017**, *17* (4), 2603–2610. https://doi.org/10.1021/acs.nanolett.7b00401

(2) Shen, L.; Pun, E. Y. B.; Ho, J. C. Recent Developments in III-V Semiconducting Nanowires for High-Performance Photodetectors. *Materials Chemistry Frontiers*. **2017**, *1,* 630–645. https://doi.org/10.1039/c6qm00279j

(3) Norouzzadeh, P.; Shakouri, A.; Vashaee, D. Valleytronics of III-V Solid Solutions for Thermoelectric Application. *RSC Adv.* **2017**, *7* (12), 7310–7314. https://doi.org/10.1039/c6ra28280f

(4) Del Alamo, J. A. Nanometre-Scale Electronics with III-V Compound Semiconductors. *Nature*. **2011**, *479,* 317–323. https://doi.org/10.1038/nature10677

(5) Lehmann, S.; Wallentin, J.; Jacobsson, D.; Deppert, K.; Dick, K. A. A General Approach for Sharp Crystal Phase Switching in InAs, GaAs, InP, and GaP Nanowires Using Only Group v Flow. *Nano Lett.* **2013**, *13* (9), 4099–4105. https://doi.org/10.1021/nl401554w

(6) Caroff, P.; Dick, K. A.; Johansson, J.; Messing, M. E.; Deppert, K.; Samuelson, L. Controlled Polytypic and Twin-Plane Superlattices in III-V Nanowires. *Nat. Nanotechnol.* **2009**, *4* (1), 50–55. https://doi.org/10.1038/nnano.2008.359

(7) Cushing, S. K.; Meng, F.; Zhang, J.; Ding, B.; Chen, C. K.; Chen, C. J.; Liu, R. S.; Bristow, A. D.; Bright, J.; Zheng, P.; et al. Effects of Defects on Photocatalytic Activity of Hydrogen-Treated Titanium Oxide Nanobelts. *ACS Catal.* **2017**, *7* (3), 1742–1748. https://doi.org/10.1021/acscatal.6b02177

(8) Wang, S. Q.; Ye, H. Q. First-Principles Study on Elastic Properties and Phase Stability of III - V Compounds. *Phys. Status Solidi Basic Res.* **2003**, *240* (1), 45–54. https://doi.org/10.1002/pssb.200301861

(9) Wilhelm, C.; Larrue, A.; Dai, X.; Migas, D.; Soci, C. Anisotropic Photonic Properties of III-V Nanowires in the Zinc-Blende and Wurtzite Phase. *Nanoscale* **2012**, *4* (5), 1446–1454. https://doi.org/10.1039/c2nr00045h

(10) Hjort, M.; Lehmann, S.; Knutsson, J.; Zakharov, A. A.; Du, Y. A.; Sakong, S.; Timm, R.; Nylund, G.; Lundgren, E.; Kratzer, P.; et al. Electronic and Structural Differences between Wurtzite and Zinc Blende Inas Nanowire Surfaces: Experiment and Theory. *ACS Nano* **2014**, *8* (12), 12346–12355. https://doi.org/10.1021/nn504795v

(11) Luo, B.; Deng, Y.; Wang, Y.; Tan, M.; Cao, L.; Zhu, W. Fabrication and Growth Mechanism of Zinc Blende and Wurtzite CdTe Nanowire Arrays with Different Photoelectric Properties. *CrystEngComm* **2012**, *14* (23), 7922–7928. https://doi.org/10.1039/c2ce25752a

(12) Alibert, C.; Joullié, A.; Joullié, A. M.; Ance, C. Modulation-Spectroscopy Study of the $Ga_{1-x}Al_xSb$ Band Structure. *Phys. Rev. B* **1983**, *27* (8), 4946–4954.

https://doi.org/10.1103/PhysRevB.27.4946

(13) Aspnes, D. E.; Olson, C. G.; Lynch, D. W. Ordering and Absolute Energies of the L6c and X6c Conduction Band Minima in GaAs. *Phys. Rev. Lett.* **1976**, *37* (12), 766–769. https://doi.org/10.1103/PhysRevLett.37.766

(14) Farr, M. K.; Traylor, J. G.; Sinha, S. K. Lattice Dynamics of GaSb. *Phys. Rev. B* **1975**, *11* (4), 1587–1594. https://doi.org/10.1103/PhysRevB.11.1587

(15) Giannozzi, P.; De Gironcoli, S.; Pavone, P.; Baroni, S. Ab Initio Calculation of Phonon Dispersions in Semiconductors. *Phys. Rev. B* **1991**, *43* (9), 7231–7242. https://doi.org/10.1103/PhysRevB.43.7231

(16) Köhl, M.; Schroth, P.; Minkevich, A. A.; Hornung, J. W.; Dimakis, E.; Somaschini, C.; Geelhaar, L.; Aschenbrenner, T.; Lazarev, S.; Grigoriev, D.; et al. Polytypism in GaAs Nanowires: Determination of the Interplanar Spacing of Wurtzite GaAs by X-Ray Diffraction. *J. Synchrotron Radiat.* **2015**, *22* (1), 67–75. https://doi.org/10.1107/S1600577514023480

(17) Kriegner, D.; Assali, S.; Belabbes, A.; Etzelstorfer, T.; Holý, V.; Schülli, T.; Bechstedt, F.; Bakkers, E. P. A. M.; Bauer, G.; Stangl, J. Unit Cell Structure of the Wurtzite Phase of GaP Nanowires: X-Ray Diffraction Studies and Density Functional Theory Calculations. *Phys. Rev. B - Condens. Matter Mater. Phys.* **2013**, *88* (11). https://doi.org/10.1103/PhysRevB.88.115315

(18) Kusch, P.; Breuer, S.; Ramsteiner, M.; Geelhaar, L.; Riechert, H.; Reich, S. Band Gap of Wurtzite GaAs: A Resonant Raman Study. *Phys. Rev. B - Condens. Matter Mater. Phys.* **2012**, *86* (7). https://doi.org/10.1103/PhysRevB.86.075317

(19) *Handbook Series on Semiconductor Parameters*; **2011**. https://doi.org/10.1142/9789812832078

(20) Madelung, O. *Semiconductors : Group IV Elements and III-V Compounds*; Springer Berlin Heidelberg, **1991**. https://doi.org/10.1007/978-3-642-45681-7

(21) Mooradian, A.; Wright, G. B. First Order Raman Effect in III-V Compounds. *Solid State Commun.* **1966**, *4* (9), 431–434. https://doi.org/10.1016/0038-1098(66)90321-8

(22) Panda, J. K.; Roy, A.; Gemmi, M.; Husanu, E.; Li, A.; Ercolani, D.; Sorba, L. Electronic Band Structure of Wurtzite GaP Nanowires via Temperature Dependent Resonance Raman Spectroscopy. *Appl. Phys. Lett.* **2013**, *103* (2). https://doi.org/10.1063/1.4813625

(23) Samara, G. A. Temperature and Pressure Dependences of the Dielectric Constants of Semiconductors. *Phys. Rev. B* **1983**, *27* (6), 3494–3505. https://doi.org/10.1103/PhysRevB.27.3494

(24) Assali, S.; Zardo, I.; Plissard, S.; Kriegner, D.; Verheijen, M. A.; Bauer, G.; Meijerink, A.; Belabbes, A.; Bechstedt, F.; Haverkort, J. E. M.; et al. Direct Band Gap Wurtzite Gallium Phosphide Nanowires. *Nano Lett.* **2013**, *13* (4), 1559–1563. https://doi.org/10.1021/nl304723c

(25) Strauch, D.; Dorner, B. Phonon Dispersion in GaAs. *J. Phys. Condens. Matter* **1990**, *2* (6), 1457–1474. https://doi.org/10.1088/0953-8984/2/6/006

(26) Wang, S. Q.; Ye, H. Q. A Plane-Wave Pseudopotential Study on III-V Zinc-Blende and Wurtzite Semiconductors under Pressure. *J. Phys. Condens. Matter* **2002**, *14* (41), 9579–9587. https://doi.org/10.1088/0953-8984/14/41/313

(27) Zardo, I.; Conesa-Boj, S.; Peiro, F.; Morante, J. R.; Arbiol, J.; Uccelli, E.; Abstreiter, G.;

Fontcuberta I Morral, A. Raman Spectroscopy of Wurtzite and Zinc-Blende GaAs Nanowires: Polarization Dependence, Selection Rules, and Strain Effects. *Phys. Rev. B - Condens. Matter Mater. Phys.* **2009**, *80* (24). https://doi.org/10.1103/PhysRevB.80.245324

(28) Zollner, S.; Garriga, M.; Humlek, J.; Gopalan, S.; Cardona, M. Temperature Dependence of the Dielectric Function and the Interband Critical-Point Parameters of GaSb. *Phys. Rev. B* **1991**, *43* (5), 4349–4360. https://doi.org/10.1103/PhysRevB.43.4349

(29) Al-Douri, Y.; Reshak, A. H. Calculated Optical Properties of GaX (X = P, As, Sb) under Hydrostatic Pressure. *Appl. Phys. A Mater. Sci. Process.* **2011**, *104* (4), 1159–1167. https://doi.org/10.1007/s00339-011-6400-6

(30) Benyahia, N.; Zaoui, A.; Madouri, D.; Ferhat, M. Dynamic Properties of III-V Polytypes from Density-Functional Theory. *J. Appl. Phys.* **2017**, *121*, 125701. https://doi.org/10.1063/1.4979011

(31) Borcherds, P. H.; Hall, R. L.; Kunc, K.; Alfrey, G. F. The Lattice Dynamics of Gallium Phosphide. *J. Phys. C Solid State Phys.* **1979**, *12*, 4699-4706. https://doi.org/10.1088/0022-3719/12/22/012

(32) Bouarissa, N.; Baaziz, H.; Charifi, Z. Electronic Properties of the Alloy System $Ga_xIn_{1-x}P_ySb_zAs_{1-y-z}$ Lattice Matched to InAs. *Phys. Status Solidi Basic Res.* **2002**, *231* (2), 403–410. https://doi.org/10.1002/1521-3951(200206)231:2<403::AID-PSSB403>3.0.CO;2-6

(33) Briki, M.; Abdelouhab, M.; Zaoui, A.; Ferhat, M. Relativistic Effects on the Structural and Transport Properties of III-V Compounds: A First-Principles Study. *Superlattices Microstruct.* **2009**, *45* (2), 80–90. https://doi.org/10.1016/j.spmi.2008.12.022

(34) Barker, A. S. Dielectric Dispersion and Phonon Line Shape in Gallium Phosphide. *Phys. Rev.* **1968**, *165* (3), 917–922. https://doi.org/10.1103/PhysRev.165.917

(35) De, A.; Pryor, C. E. Predicted Band Structures of III-V Semiconductors in the Wurtzite Phase. *Phys. Rev. B - Condens. Matter Mater. Phys.* **2010**, *81*, 199901. https://doi.org/10.1103/PhysRevB.81.155210

(36) Nakamura, S.; Senoh, M.; Mukai, T. P-Gan/n-Ingan/n-Gan Double-Heterostructure Blue-Light-Emitting Diodes. *Jpn. J. Appl. Phys.* **1993**, *32* (1 A), L8–L11. https://doi.org/10.1143/JJAP.32.L8

(37) Dimroth, F.; Grave, M.; Beutel, P.; Fiedeler, U.; Karcher, C.; Tibbits, T. N. D.; Oliva, E.; Siefer, G.; Schachtner, M.; Wekkeli, A.; et al. Wafer Bonded Four-Junction GaInP/GaAs//GaInAsP/GaInAs Concentrator Solar Cells with 44.7% Efficiency. *Prog. Photovoltaics Res. Appl.* **2014**, *22* (3), 277–282. https://doi.org/10.1002/pip.2475

(38) Leem, J. W.; Yu, J. S. Artificial Inverted Compound Eye Structured Polymer Films with Light-Harvesting and Self-Cleaning Functions for Encapsulated III-V Solar Cell Applications. *RSC Adv.* **2015**, *5* (75), 60804–60813. https://doi.org/10.1039/c5ra05991g

(39) Bosi, M.; Pelosi, C. The Potential of III-V Semiconductors as Terrestrial Photovoltaic Devices. *Prog. Photovoltaics Res. Appl.* **2007**, *15* (1), 51–68. https://doi.org/10.1002/pip.715

(40) Shur M. *Handbook Series on Semiconductor Parameters*; **2011**; Vol. 1. https://doi.org/10.1142/9789812832078

(41) Varadhan, P.; Fu, H. C.; Priante, D.; Retamal, J. R. D.; Zhao, C.; Ebaid, M.; Ng, T. K.; Ajia, I.; Mitra, S.; Roqan, I. S.; et al. Surface Passivation of GaN Nanowires for Enhanced

Photoelectrochemical Water-Splitting. *Nano Lett.* **2017**, *17* (3), 1520–1528. https://doi.org/10.1021/acs.nanolett.6b04559

(42) Mingo, N. Thermoelectric Figure of Merit and Maximum Power Factor in III-V Semiconductor Nanowires. *Appl. Phys. Lett.* **2004**, *84* (14), 2652–2654. https://doi.org/10.1063/1.1695629

(43) Bahk, J. H.; Bian, Z.; Zebarjadi, M.; Zide, J. M. O.; Lu, H.; Xu, D.; Feser, J. P.; Zeng, G.; Majumdar, A.; Gossard, A. C.; et al. Thermoelectric Figure of Merit of $(In_{0.53}Ga_{0.47}As)_{0.8}(In_{0.52}Al_{0.48}As)_{0.2}$ III-V Semiconductor Alloys. *Phys. Rev. B - Condens. Matter Mater. Phys.* **2010**, *81* (23). https://doi.org/10.1103/PhysRevB.81.235209

(44) Giannozzi, P.; Baroni, S.; Bonini, N.; Calandra, M.; Car, R.; Cavazzoni, C.; Ceresoli, D.; Chiarotti, G. L.; Cococcioni, M.; Dabo, I.; et al. QUANTUM ESPRESSO: A Modular and Open-Source Software Project for Quantum Simulations of Materials. *J. Phys. Condens. Matter* **2009**, *21*(39), 395502. https://doi.org/10.1088/0953-8984/21/39/395502

(45) Perdew, J. P.; Zunger, A. Self-Interaction Correction to Density-Functional Approximations for Many-Electron Systems. *Phys. Rev. B* **1981**, *23* (10), 5048–5079. https://doi.org/10.1103/PhysRevB.23.5048

(46) Pack, J. D.; Monkhorst, H. J. "special Points for Brillouin-Zone Integrations"-a Reply. *Phys. Rev. B* **1977**, *16* (4), 1748–1749. https://doi.org/10.1103/PhysRevB.16.1748

(47) Baroni, S.; De Gironcoli, S.; Dal Corso, A.; Giannozzi, P. Phonons and Related Crystal Properties from Density-Functional Perturbation Theory. *Reviews of Modern Physics*. **2001**, *73*, 515–562. https://doi.org/10.1103/RevModPhys.73.515

(48) Caroff, P.; Bolinsson, J.; Johansson, J. Crystal Phases in III-V Nanowires: From Random toward Engineered Polytypism. *IEEE Journal on Selected Topics in Quantum Electronics*. **2011**, *17*(4), 829–846. https://doi.org/10.1109/JSTQE.2010.2070790

(49) Gajdoš, M.; Hummer, K.; Kresse, G.; Furthmüller, J.; Bechstedt, F. Linear Optical Properties in the Projector-Augmented Wave Methodology. *Phys. Rev. B - Condens. Matter Mater. Phys.* **2006**, *73* (4), 045112. https://doi.org/10.1103/PhysRevB.73.045112

(50) Harl, J.; Kresse, G.; Sun, L. D.; Hohage, M.; Zeppenfeld, P. Ab Initio Reflectance Difference Spectra of the Bare and Adsorbate Covered Cu(110) Surfaces. *Phys. Rev. B - Condens. Matter Mater. Phys.* **2007**, *76* (3), 035436. https://doi.org/10.1103/PhysRevB.76.035436

(51) O. Madelung and Landot Bornstein. Properties of Group IV Elements and III-V, II-V, and I-VII Compounds. *Numer. Data Funct. Relationships Sci. Technol.* **1982**, *17a* (2019), 9. https://doi.org/10.1007/978-3-642-45681-7

(52) Haas, P.; Tran, F.; Blaha, P. Calculation of the Lattice Constant of Solids with Semilocal Functionals. *Phys. Rev. B - Condens. Matter Mater. Phys.* **2009**, *79* (8), 085104. https://doi.org/10.1103/PhysRevB.79.085104

(53) Tomić, S.; Montanari, B.; Harrison, N. M. The Group III-V's Semiconductor Energy Gaps Predicted Using the B3LYP Hybrid Functional. *Phys. E Low-Dimensional Syst. Nanostructures* **2008**, *40* (6), 2125–2127. https://doi.org/10.1016/j.physe.2007.10.022

(54) Wang, Y.; Shang, S. L.; Fang, H.; Liu, Z. K.; Chen, L. Q. First-Principles Calculations of Lattice Dynamics and Thermal Properties of Polar Solids. *npj Computational Materials*. **2016**, *2*, 16006. https://doi.org/10.1038/npjcompumats.2016.6

(55) Manjón, F. J.; Errandonea, D.; Romero, A. H.; Garro, N.; Serrano, J.; Kuball, M. Lattice

Dynamics of Wurtzite and Rocksalt AlN under High Pressure: Effect of Compression on the Crystal Anisotropy of Wurtzite-Type Semiconductors. *Phys. Rev. B - Condens. Matter Mater. Phys.* **2008**, *77* (20), 205204. https://doi.org/10.1103/PhysRevB.77.205204

(56) Borcherds, P. H.; Hall, R. L.; Kunc, K.; Alfrey, G. F. The Lattice Dynamics of Gallium Phosphide. *J. Phys. C Solid State Phys.* **1979**, *12* (22), 4699–4706. https://doi.org/10.1088/0022-3719/12/22/012

(57) Singh, D.; Mazin, I. Calculated Thermoelectric Properties of La-Filled Skutterudites. *Phys. Rev. B - Condens. Matter Mater. Phys.* **1997**, *56*(4), R1650. https://doi.org/10.1103/PhysRevB.56.R1650

(58) Bardeen, J.; Shockley, W. Deformation Potentials and Mobilities in Non-Polar Crystals. *Phys. Rev.* **1950**, *80* (1), 72–80. https://doi.org/10.1103/PhysRev.80.72

(59) O. Madelung and Landot Bornstein. Properties of Group IV Elements and III-V, II-V, and I-VII Compounds. *Numer. Data Funct. Relationships Sci. Technol.* **1982**, *17a*

(60) Adachi, S. Lattice Thermal Conductivity of Group-IV and III-V Semiconductor Alloys. *J. Appl. Phys.* **2007**, *102* (6), 063502. https://doi.org/10.1063/1.2779259

(61) Steigmeier, E. F.; Kudman, I. Acoustical-Optical Phonon Scattering in Ge, Si, and III-V Compounds. *Phys. Rev.* **1966**, *141* (2), 767–774. https://doi.org/10.1103/PhysRev.141.767

(62) Muzhdaba, V. M.; Nashel'skii, A. Y.; Tamarin, P. V.; Shalyt, S. S. Thermal Conductivity and Thermo-Emf of AlSb and GaP at Low Temperatures. *Sov. Phys. Solid State* **1969**, *10* (10), 2265–2266.

(63) Inyushkin, A. V.; Taldenkov, A. N.; Yakubovsky, A. Y.; Markov, A. V.; Moreno-Garsia, L.; Sharonov, B. N. Thermal Conductivity of Isotopically Enriched 71GaAs Crystal. *Semicond. Sci. Technol.* **2003**, *18* (7), 685–688. https://doi.org/10.1088/0268-1242/18/7/315

(64) Madsen, G. K. H.; Singh, D. J. BoltzTraP. A Code for Calculating Band-Structure Dependent Quantities. *Comput. Phys. Commun.* **2006**, *175* (1), 67–71. https://doi.org/10.1016/j.cpc.2006.03.007

(65) Holland, M. G. Analysis of Lattice Thermal Conductivity. *Phys. Rev.* **1963**, *132* (6), 2461–2471. https://doi.org/10.1103/PhysRev.132.2461

(66) Lindsay, L.; Broido, D. A.; Reinecke, T. L. Thermal Conductivity and Large Isotope Effect in GaN from First Principles. *Phys. Rev. Lett.* **2012**, *109* (9), 095901. https://doi.org/10.1103/PhysRevLett.109.095901

(67) Mukhopadhyay, S.; Stewart, D. A. First-Principles Study of the Phonon Dispersion and Dielectric Properties of Wurtzite InP: Role of in 4 d Electrons. *Phys. Rev. B - Condens. Matter Mater. Phys.* **2014**, *89* (5), 054302. https://doi.org/10.1103/PhysRevB.89.054302

(68) Morelli, D. T.; Slack, G. A. High Lattice Thermal Conductivity Solids. In *High Thermal Conductivity Materials*; **2006**; pp 37–68. https://doi.org/10.1007/0-387-25100-6_2

(69) Dabhi, S. D.; Jha, P. K. Ab Initio Study of Strained Wurtzite InAs Nanowires: Engineering an Indirect-Direct Band Gap Transition through Size and Uniaxial Strain. *RSC Adv.* **2015**, *5* (109), 89993–90000. https://doi.org/10.1039/c5ra16512a

(70) Copple, A.; Ralston, N.; Peng, X. Engineering Direct-Indirect Band Gap Transition in Wurtzite GaAs Nanowires through Size and Uniaxial Strain. *Appl. Phys. Lett.* **2012**, *100* (19), 193108. https://doi.org/10.1063/1.4718026

(71) Peng, X.; Copple, A. Origination of the Direct-Indirect Band Gap Transition in Strained Wurtzite and Zinc-Blende GaAs Nanowires: A First Principles Study. *Phys. Rev. B - Condens. Matter Mater. Phys.* **2013**, *87* (11), 115308. https://doi.org/10.1103/PhysRevB.87.115308

(72) del Alamo, J. A. Nanometre-Scale Electronics with III–V Compound Semiconductors. *Nature* **2011**, *479* (7373), 317–323. https://doi.org/10.1038/nature10677

(73) Hang, Q.; Wang, F.; Carpenter, P. D.; Zemlyanov, D.; Zakharov, D.; Stach, E. A.; Buhro, W. E.; Janes, D. B. Role of Molecular Surface Passivation in Electrical Transport Properties of InAs Nanowires. *Nano Lett.* **2008**, *8* (1), 49–55. https://doi.org/10.1021/nl071888t

(74) Martinez-Garcia, A.; Russell, H. B.; Paxton, W.; Ravipati, S.; Calero-Barney, S.; Menon, M.; Richter, E.; Young, J.; Deutsch, T.; Sunkara, M. K. Unassisted Water Splitting Using a $GaSb_xP_{(1-x)}$ Photoanode. *Adv. Energy Mater.* **2018**, *8* (16), 1703247. https://doi.org/10.1002/aenm.201703247

(75) dos Santos, C. L.; Piquini, P.; Magri, R. Band Folding, Strain, Confinement, and Surface Relaxation Effects on the Electronic Structure of GaAs and GaP: From Bulk to Nanowires. *Eur. Phys. J. B* **2019**, *92* (9), 1-11. https://doi.org/10.1140/epjb/e2019-100288-y

(76) Peng, W.; Jabeen, F.; Jusserand, B.; Harmand, J. C.; Bernard, M. Conduction Band Structure in Wurtzite GaAs Nanowires: A Resonant Raman Scattering Study. *Appl. Phys. Lett.* **2012**, *100*, 073102. https://doi.org/10.1063/1.3684837

(77) Vukajlovic-Plestina, J.; Kim, W.; Ghisalberti, L.; Varnavides, G.; Tütüncuoglu, G.; Potts, H.; Friedl, M.; Güniat, L.; Carter, W. C.; Dubrovskii, V. G.; et al. Fundamental Aspects to Localize Self-Catalyzed III-V Nanowires on Silicon. *Nat. Commun.* **2019**, *10* (1), 1-7. https://doi.org/10.1038/s41467-019-08807-9

(78) Minami, Y.; Yoshida, A.; Motohisa, J.; Tomioka, K. Growth and Characterization of GaAs Nanowires on Ge(1 1 1) Substrates by Selective-Area MOVPE. *J. Cryst. Growth* **2019**, *506*, 135–139. https://doi.org/10.1016/j.jcrysgro.2018.10.009

---